

Energy conversion in Purple Bacteria Photosynthesis

Chapter to appear in *Photosynthesis*, INTECH, 2011

Felipe Caycedo-Soler^{1,2}, Ferney J. Rodríguez², Luis Quiroga²,
Guannan Zhao³ and Neil F. Johnson³

¹*Ulm University, Institute of Theoretical Physics, Ulm, Germany*

²*Departamento de Física, Universidad de los Andes, Bogotá, Colombia*

³*Department of Physics, University of Miami, Coral Gables, Miami, Florida, USA*

Introduction

The study of how photosynthetic organisms convert light offers insight not only into nature's evolutionary process, but may also give clues as to how best to design and manipulate artificial photosynthetic systems – and also how far we can drive natural photosynthetic systems beyond normal operating conditions, so that they can harvest energy for us under otherwise extreme conditions. In addition to its interest from a basic scientific perspective, therefore, the goal to develop a deep quantitative understanding of photosynthesis offers the potential payoff of enhancing our current arsenal of alternative energy sources for the future.

In the following Chapter, we consider the excitation dynamics of photosynthetic membranes in *Rps. Photometricum* purple bacteria. The first studies on purple bacteria photosynthetic membranes were concerned with the complex underlying detailed structure [19, 27, 32, 45]. The interested reader might find helpful the first section of this chapter where we present a summary of structures and processes that allow photosynthesis in purple bacteria. As improved resolution became available for light-harvesting structures, so too the community's interest increased in understanding the details of the rapid femto- to picosecond timescales for the excitation transfer process within a given harvesting complex – even to the regime where quantum effects are expected. Indeed such quantum effects have recently been confirmed in, for instance, the Fenna-Matthews-Olson complex of green sulfur bacteria [9]. However, the processes occurring at this level of detail in terms of both structure and properties of the excitation harvesting, have not yet been shown as being crucial to the performance of the full harvesting membrane, nor with the primary goal of any given photosynthetic organism: to fuel its metabolism. We focus on the transfer among different complexes, in particular the inter-complex excitation transfer. We consider first a system of few complexes in order to understand the consequences on the dynamics of the complexes' connectedness. We also consider the relative amounts of harvesting complexes (i.e. stoichiometry) on small sized networks in order to help establish our understanding of the behavior of complete chromatophore vesicles.

As a whole, chromatophore vesicles comprise sections of the purple bacteria cytoplasmic membrane where a large number of harvesting complexes accommodate. The current capabilities to dissect these vesicles on the nanoscale through Atomic Force Microscopy (AFM) has provided evidence of changes in the conformation of chromatophores as a result of different environmental conditions. According to Ref.[34], membranes grown under Low Light Intensity (LLI, 10 Watt/m²) present a relative amount of harvesting complexes which is different to the stoichiometry observed for bacteria grown under High Light Intensity (HLI, 100 Watt/m²), thereby pinpointing the importance of global changes in the complete vesicles as an important means of fulfilling the bacteria's metabolic requirements. In order to study these global conformational changes – given the fact that the inter-complex transfer time-scale involves several picoseconds and the excitation delocalization length is not expected to be beyond a single harvesting complex – we choose a model of excitation dynamics which is based on a classical random walk. This random walk is coupled to the main processes leading to electron/chemical energy transformation, and hence the bacteria's metabolic demands.

This Chapter is organized as follows. Section 1 provides a review of the basic structures involved in excitation transfer, along with a summary of the processes required for electron/chemical energy conversion. A discussion of the dynamics of excitations in a few model architectures is explored in section 2, in order to understand the results from complete LLI and HLI adapted chromatophores in section 3 and to guide our development of an analytical model in section 4 for determining both the efficiency and power output of any given chromatophore vesicle under arbitrary light intensity regimes. Lastly, in section 5 we explore the effect of incident light with extreme photon arrival statistics, on the resulting electronic/chemical energy conversion, in order to heuristically provide a survivability margin beyond which terrestrial bacteria could not survive. This is motivated by the fact that one day, it may be necessary to send simple bacteria into deep space and/or cope with extreme photon conditions here on Earth as a result of a catastrophic solar change.

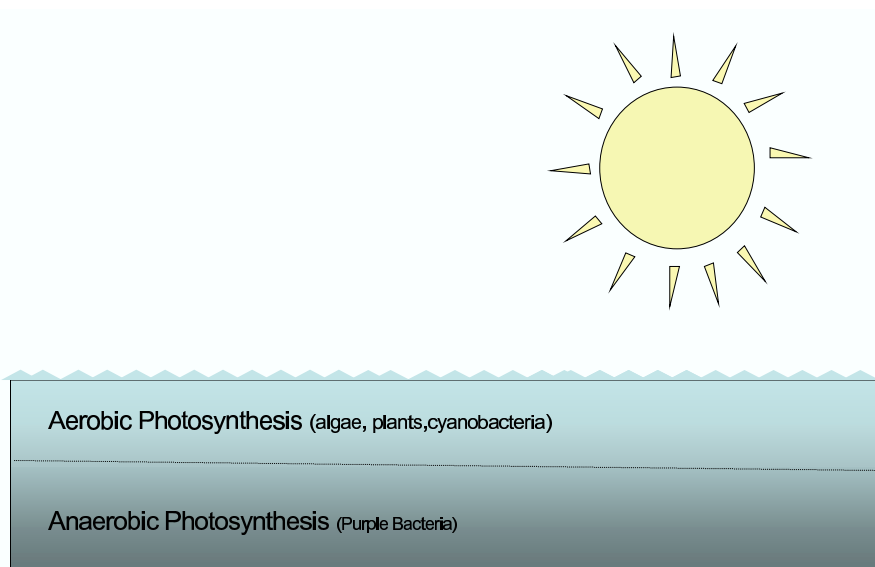


FIG. 1: Representation of a lake containing both aerobic and anaerobic phototrophic organisms. Note that purple bacterial photosynthesis is restricted to the lower anaerobic layer and so they only receive solar energy that has been filtered, mainly by chlorophylls belonging to algae, cyanobacteria and plants.

1. Important processes for solar/chemical energy conversion

Purple bacteria sustain their metabolism using photosynthesis in anaerobic conditions and under the dim light excitation proper of several meters deeps at ponds, lagoons and streams [30]. As depicted in Fig.1, aerobic organisms are present near the surface of water reservoirs, collect blue and red spectral components of sun's light, leaving only the green and far red ($> 750\text{nm}$) components, from where purple bacteria must fulfill their energy requirements.

The light energy absorption is accomplished through intracytoplasmic membranes where different pigment-protein complexes accommodate. Light Harvesting complexes (LHs) have the function of absorbing light and transfer it to Reaction Centers (RCs), where a charge separation process is initiated [7]. The unpaired charge reduces a quinone, which using a periplasmic hydrogen, converts to quinol (Q_BH_2). RCs neutrality is reestablished thanks to cytochrome *cyt* charge carrier, which after undocking from the RC, must find the bc_1 complex to receive an electron and start its cycle all over again. The electron in bc_1 is given due to cytoplasmic Quinol delivery in bc_1 . The proton gradient induced by the charge carriers cycling becomes the precursor of adenosyn triphosphate (ATP) synthesis: $\text{ADP} + \text{P} \rightarrow \text{ATP} + \text{Energy}$, where ADP and P refer respectively, to adenosine diphosphate and phosphorous. The cycle is depicted in Fig.2.

1.1 Harvesting function

Light absorption occurs through organic molecules, known as chromophores, inserted in protein complexes. Bacteriochlorophylls (BChl) and carotenoids (Car) chromophores are the main absorbers in purple bacteria photosynthesis, principally in the far red and green, respectively. The light absorption process occurs through chromophore's Qy electronic transition excitation. Several chromophores are embedded in protein helices, named α and β apoproteins, inside complexes, classified by their absorption spectral maximum. Light Harvesting complex 2 (LH2) reveals two concentric subunits that according to their absorption maxima are called B800 or B850, composed of nine pairs of apoproteins [27] comprising an inner α -helix and an outer β -helix both crossing the harvesting membrane from periplasm to cytoplasm, in an $\alpha\beta$ unit that serves to anchor a highly interacting B850 dimer and one B800 chromophore. Hence, the B800 is composed of nine chromophores, while B850 include eighteen BChl a chromophores, having dipole moments parallel and nearly perpendicular to the membrane plane, respectively. Raman spectra using different excitation wavelength [13] and stoichiometry analysis [1], indicated that one carotenoid (Car) is present per each $\alpha\beta$ unit. Light Harvesting complex 1 (LH1) absorbs maximally at 883 nm, and contain 32 BChls, arranged in 16 bi-chromophore $\alpha\beta$ units, surrounding an RC [22] in the same geometrical arrangement as B850 chromophores. An

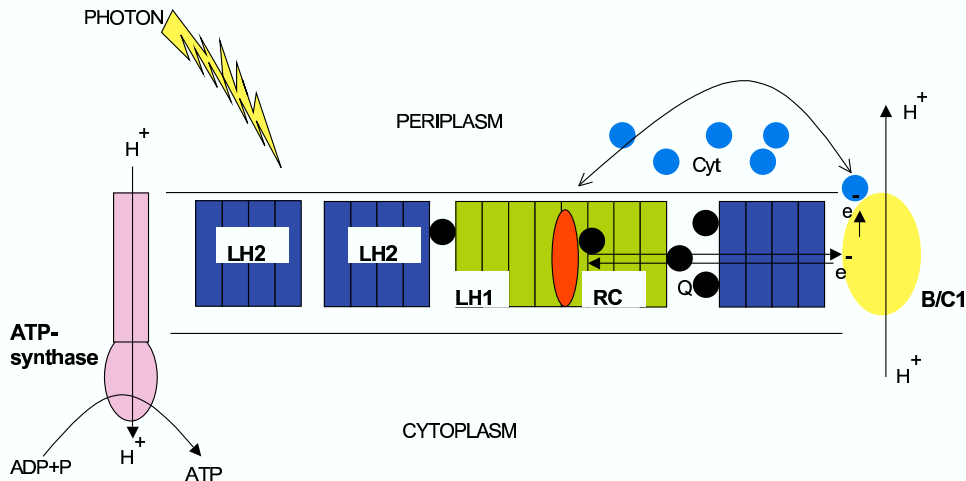


FIG. 2: Schematic representation of the photosynthetic apparatus in the intracytoplasmic membrane of purple bacteria. The reaction center (RC, red) is surrounded by the light-harvesting complex 1 (LH1, green) to form the LH1+RC complex, which is surrounded by multiple light-harvesting complexes (LH2s) (blue), forming altogether the photosynthetic unit (PSU). Photons are absorbed by LHs and excitation is transferred to the RC initiating a charge (electron-hole) separation. Electrons are shuttled back by the cytochrome c_2 charge carrier (blue) from the ubiquinone-cytochrome bc_1 complex (yellow) to the RC. The electron transfer across the membrane produces a proton gradient that drives the synthesis of ATP from ADP by the ATPase (orange). Electron e^- is represented in blue, and quinones Q_B , likely confined to the intramembrane space, in black.

RC presents a highly interacting dimer, the special pair (P), that is ionized due to the electronic excitation transferred from the surrounding LH1.

The complexes' photon absorption cross section has been calculated for LH1 and LH2 complexes, where all absorbing molecules and extinction coefficients [12] have been taken into account. A photon of wavelentht λ , is part of the power spectrum of a source with occupation numbers $n(\lambda)$. Normalized to 18 W/m^2 intensity, the rate of photon absorption for circular LH1 complexes in *Rb. sphaeroides* [14]:

$$\gamma_1^A = \int n(\lambda) \sigma_{\text{LH1}}(\lambda) d\lambda = 18 \text{ s}^{-1}. \quad (1)$$

The same procedure applied to LH2 complexes, yields a photon capture rate of $\gamma_2^A = 10 \text{ s}^{-1}$. Since these rates are normalized to 18 W/m^2 , the extension to arbitrary light intensity I is straightforward. The rate of photon absorption normalized to 1 W/m^2 intensity, will be $\gamma_{1(2)} = 1(0.55) \text{ s}^{-1}$. From now on, subindexes 1 and 2 relate to quantities of LH1 and LH2 complexes, respectively. Vesicles containing several hundreds of complexes will have an absorption rate:

$$\gamma_A = I(\gamma_1 N_1 + \gamma_2 N_2) \quad (2)$$

where $N_{1(2)}$ is the number of LH1 (LH2) complexes in the vesicle.

1.2 Excitation transfer

Excitation transfer happens through Coulomb interaction of electrons, excited to the Q_y electronic transition in chromophores. The interaction energy can be formally written [41]:

$$V_{ij} = \frac{1}{2} \sum_{m,n,p,q} \sum_{\sigma,\sigma'} \langle \phi_m \phi_n | V | \phi_p \phi_q \rangle c_{m\sigma}^+ c_{p\sigma'}^+ c_{q\sigma} c_{n\sigma}, \quad (3)$$

where $c_{m\sigma}^+$, $c_{n\sigma'}$ are fermion creation and annihilation operators of electrons with spin σ and σ' , in the mutually orthogonal atomic orbitals ϕ_m and ϕ_n . The overlap $\langle \phi_m \phi_n | V | \phi_p \phi_q \rangle$ is the Coulomb integral:

$$\langle \phi_m \phi_p | V | \phi_n \phi_q \rangle = \int \int d\vec{r}_1 d\vec{r}_2 \phi_m^*(\vec{r}_1 - \vec{r}_i) \phi_p(\vec{r}_1 - \vec{r}_i) \frac{e^2}{|\vec{r}_1 - \vec{r}_2|} \phi_n^*(\vec{r}_2 - \vec{r}_j) \phi_q(\vec{r}_2 - \vec{r}_j) \quad (4)$$

that accounts on inter-molecular exchange contribution when donor and acceptor are at a distance comparable to the extent of the molecules, and the direct Coulomb contribution for an electron that makes a transition between ϕ_m and ϕ_p , having both a finite value near the position of the donor $\vec{r}_1 \approx \vec{r}_D$, while another electron is excited between ϕ_n and ϕ_q at the acceptor coordinate $\vec{r}_2 \approx \vec{r}_A$. In this latter situation, a commonly used framework concerns a tight-binding Hamiltonian, where details in the specific molecular orbitals $|\phi_n\rangle$ involving mainly the Q_y orbitals is left aside, and emphasis relies on occupation with a single index labeling an electronic state $|i\rangle$ concerning occupation in a given chromophore. The Hamiltonian H in the chromophore site basis $|i\rangle$,

$$H = \epsilon \sum_i |i\rangle \langle i| + \sum_{i,j} V_{ij} |i\rangle \langle j| \quad (5)$$

has diagonal elements $\langle i | H | i \rangle = \epsilon$, concerning the energy of the excitation, usually measured from the ground electronic state. Neighboring chromophores are too close to neglect their charge distribution and its interaction is determined such that the effective Hamiltonian spectrum matches the spectrum of an extensive quantum chemistry calculation [18]. In the LH2 complex, the B850 ring, with nearest neighbors coupling $\langle i | H | i + 1 \rangle = 806 \text{ cm}^{-1}$ or 377 cm^{-1} for chromophores respectively, within or in different neighboring $\alpha\beta$ units. For next-to-neighboring chromophores the dipole-dipole approximation is usually used,

$$\begin{aligned} \langle i | H | j \rangle &= V_{ij} = C \left(\frac{\vec{\mu}_i \cdot \vec{\mu}_j}{r_{ij}^3} - \frac{3(\vec{r}_{ij} \cdot \vec{\mu}_i)(\vec{r}_{ij} \cdot \vec{\mu}_j)}{r_{ij}^5} \right) \\ &\text{with } i \neq j, i = j \neq \pm 1 \end{aligned} \quad (6)$$

where $\vec{\mu}_i$ is the dipole moment and r is the distance between the interacting dipoles with constants: $\epsilon = 13059 \text{ cm}^{-1}$ and $C = 519044 \text{ \AA}^3 \text{ cm}^{-1}$. The LH1 complex has a spectrum maximum near 875 nm, with inter-complex distances and nearest neighbor interactions equal to the ones provided in the B850 LH2 ring. The molecular nature of chromophores involve vibrational degrees of freedom that provide a manifold within each electronic states which should be accounted. However, given these parameters within a harvesting complex, intra-complex energy transfer involves sub-picosecond time-scales, that imply relevance of electronic quantum features over the influence of thermalization in the vibrational manifold. If decoherence sources are not important within the time-scale of excitation dynamics on donor or acceptor aggregates, they can be known from the eigenvector problem $H|\phi_k\rangle = E_k|\phi_k\rangle$ whose solution provides excitonic fully delocalized states

$$|\phi_k\rangle = \sum_n a_{k,i} |i\rangle \quad (7)$$

considered to best describe the B850 ring. A slightly less interaction strength allows thermalization through the vibrational manifold in comparable time-scales, degrading delocalization in the B800 ring over 2-3 pigments, however, able to improve robustness of B800→B850 energy transfer [20].

The fact that states involved in excitation transfer in molecules include the vibrational manifold, makes enormous the Hilbert space over which the sums of eq.(3) should be formally performed. When the transfer occurs with chromophores that belong to different complexes, say inter-complex energy transfer, rapid thermalization out stands direct Coulomb mechanism, and no defined phase relationship between donor and acceptor electronic states is expected. The hermitian nature of excitonic exchange is replaced due to decoherence, by a rate to describe electronic excitation transfer within thermalization in the vibrational manifold. According to Fermi's golden rule, adapted to the vibrational continuum, the rate of transfer is given by [17]:

$$k_{DA} = \frac{2\pi}{\hbar} \int dE \int_{E_{A_0}} d\omega_A \int_{E_{D_0}^*} d\omega_D \frac{g_D^*(\omega_D^*) \exp(-\omega_D^*/k_B T)}{Z_D^*} \frac{g_A(\omega_A) \exp(-\omega_A/k_B T)}{Z_A} |\tilde{U}_{DA}|^2 \quad (8)$$

interpreted as a the sum of Coulomb contributions from electrons at donor (D) and acceptor (A) aggregates in ground or excited states (these latter denoted by *), $\tilde{U}_{DA} = \langle \Psi_{D^*} \Psi_A | V_{DA} | \Psi_D \Psi_{A^*} \rangle$, weighted by Boltzmann factor

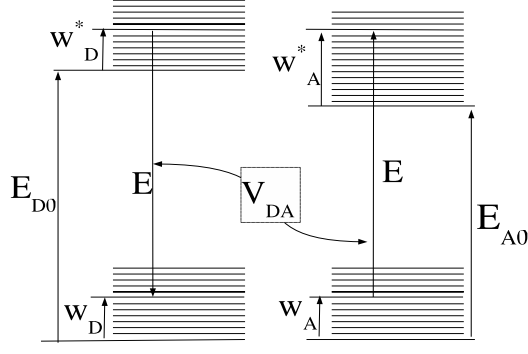


FIG. 3: Energy level scheme of donor and acceptor molecules. Although the zero phonon line might be different between both, energy conservation on the transfer applies due to vibrational levels.

(k_B is Boltzmann constant) and vibrational manifold multiplicity ($g_{D(A)}(w_{D(A)})$ for donor (acceptor)) at the electronic energies $w_{D(A)}$ measured from the donor (acceptor) zero phonon lines $E_{D(A)0}$. With the Born-Oppenheimer approximation [17, 41] $|\Psi\rangle$ is assumed as products of electronic $|\phi\rangle$ and vibrational $|\chi\rangle$ molecular states:

$$\begin{aligned}\hat{U}_{DA} &\approx \langle \phi_{D^*} \phi_A | V_{DA} | \phi_D \phi_{A^*} \rangle \times \langle \chi(w_D^*) | \chi(w_D) \rangle \langle \chi(w_A) | \chi(w_A^*) \rangle \\ &\approx U_{DA} \langle \chi(w_D^*) | \chi(w_D) \rangle \langle \chi(w_A) | \chi(w_A^*) \rangle\end{aligned}\quad (9)$$

where $U_{DA} = \langle \phi_{D^*} \psi_A | V_{DA} | \psi_D \psi_{A^*} \rangle$. Using the above approximation, the expression (8) now including the overlap between vibrational levels can be cast in a more illustrative form:

$$k_{DA} = \frac{2\pi}{\hbar} |U_{DA}|^2 \int dE G_D(E) G_A(E) \quad (10)$$

Here, $G_D(E)$ and $G_A(E)$ are often called the Franck-Condon weighted and thermally averaged combined density of states. Explicitly:

$$G_D(E) = \int_{E_{D_0^*}} dw_D^* \frac{g_D^*(w_D^*) \exp(-w_D^*/k_B T) |\langle \chi(w_D^*) | \chi(w_D) \rangle|^2}{Z_D^*}$$

with equal expression for acceptor molecule by replacement $D \rightarrow A$. Förster showed [11] that these distributions are related to extinction coefficient $\epsilon(E)$ and fluorescence spectrum $f_D(E)$ of direct experimental verification:

$$\epsilon(E) = \frac{2\pi N_0}{3 \ln 10 \hbar^2 n c} |\mu_A|^2 E G_A(E), \quad f_D(E) = \frac{3\hbar^4 c^3 \tau_0}{4n} |\mu_D|^2 E^3 G_D(E) \quad (11)$$

where $N_0 = 6.022 \times 10^{20}$ is the number of molecules per mol per cm^3 , n is the refractive index of the molecule sample, c the speed of light, and τ_0 the mean fluorescence time of the donor excited state. For normalized spectra

$$\hat{\epsilon}_A(E) = \frac{\epsilon_A(E)}{\int dE \epsilon_A(E)/E}, \quad \hat{f}_D(E) = \frac{f_D(E)}{\int dE f_D(E)/E^3} \quad (12)$$

and from the relations $w_D = E_{D_0^*} + w_D^* - E$ and $w_A^* = -E_{A_0} + w_A + E$ schematically presented in Fig.3, the Förster rate is cast

$$k_{DA} = \frac{2\pi}{\hbar} |U_{DA}|^2 \int dE \frac{\hat{\epsilon}_A(E) \hat{f}_D(E)}{E^4}. \quad (13)$$

Therefore, whenever fluorescence and absorption spectra are available, an estimate for the excitation transfer rate can be calculated.

Thermalization occurs firstly in the vibrational manifold of the electronic states involved. Due to the greater energy gap of electronic transitions compared with the one of vibrational nature, on a longer time-scale thermalization also occurs in excitonic states. Accordingly, the calculation in eq.(9) involves an statistical thermal mixture, explicitly:

$$\rho = \frac{1}{\text{Tr}\{\cdot\}} \sum_k \exp(-E_k/k_B T) |\phi_k\rangle \langle \phi_k| \quad (14)$$

where $\text{Tr}\{\cdot\}$ is trace of the numerator operator, used to normalize the state. Hence, in a straightforward fashion

$$\begin{aligned}
 U_{DA} = \text{Tr}\{\rho V_{DA}\} &= \frac{1}{\sum_k \exp(-E_k/k_B T)} \sum_k \sum_p \exp(-E_k/k_B T) \langle \phi_k | V_{DA} | \phi_p \rangle \\
 &= \frac{1}{\sum_k \exp(-E_k/k_B T)} \sum_{k,p,i,j} a_{k,i} a_{p,j}^* V_{ij}
 \end{aligned} \tag{15}$$

where the element $\langle \phi_k | V_{DA} | \phi_p \rangle$ are the elements of interaction among exciton states in molecules on different complexes and use is made of the individual contributions of excitonic states in chromophore's site basis eq.(7).

Summarizing, excitation transfer occurs through induced dipole transfer, among BChls transitions. The common inter-complex BChl distances 20-100 Å [2, 34] cause excitation transfer to arise through the Coulomb interaction on the picosecond time-scale [17], while vibrational dephasing destroys coherences within a few hundred femtoseconds [23, 29]. As noted, the Coulomb interaction as dephasing occurs, makes the donor and acceptor phase become uncorrelated pointing into a classical rate behavior. Transfer rate measures from pump-probe experiments agree with the just outlined generalized Förster calculated rates [17], assuming intra-complex delocalization along thermodynamical equilibrium. LH2→LH2 transfer has not been measured experimentally, although an estimate of $t_{22} = 10$ ps has been calculated [17]. LH2→LH1 transfer has been measured for *R. Sphaeroides* as $t_{21} = 3.3$ ps [16]. Due to formation of excitonic states [21], back-transfer LH1→LH2 is enhanced as compared to the canonical equilibrium rate for a two-level system, up to a value of $t_{12} = 15.5$ ps. The LH1→LH1 mean transfer time t_{11} has not been measured, but the just mentioned generalized Förster calculation [31] has reported an estimated mean time t_{11} of 20 ps. LH1→RC transfer occurs due to ring symmetry breaking through optically forbidden (within ring symmetry) second and third lowest exciton lying states [18], as suggested by agreement with the experimental transfer time of 35-37 ps at 77 K [43, 44]. Increased spectral overlap at room temperature improves the transfer time to $t_{1,RC} = 25$ ps [42]. A photo-protective design makes the back-transfer from an RC's fully populated lowest exciton state to higher-lying LH1 states occur in a calculated time of $t_{RC,1} = 8.1$ ps [18], close to the experimentally measured 7-9 ps estimated from decay kinetics after RC excitation [40].

Table I shows the results of mean transfer times presented in Ref.[31] through the above mentioned calculation, compared with the experimental evidence restricted to different complex kind from the spectral resolution requirement of pump-probe spectroscopy. Since LH1↔LH1 and LH2↔LH2 transfer steps involve equal energy transitions, no experimental evidence is available regarding the rate at which these transitions occur. The experimentally determined B800→B850 rate was 1/700fs [38]. The inter-complex transfer rate between LH2→LH1 have been determined experimentally to be 1/3.3ps [16]. Experimentally, LH1↔RC forward transfer rate ranges between 1/50ps and 1/35ps, while back-transfer rate ranges between 1/12ps and 1/8ps [39, 40, 43]. It is interesting to note that exists a two fold difference in the experimental and theoretical determined LH2→LH1, ascribed to BChla Q_y dipole moment underestimation. It is assumed for theoretical calculation a value of 6.3 Debye, while a greater BChla Q_y dipole moment in *Prostecochloris aestuarii* (not a purple bacterium) of 7.7 Debye has been determined [31]. On the other hand, LH1→RC theoretical calculation gives a greater value for transfer rate, thought to arise due to an overestimate of LH1 exciton delocalization [31]. This rate decreases when delocalization is assumed over fewer BChl's, therefore, further research is needed to understand the effect of decoherence sources (static inhomogeneities and dynamical disorder due to thermal fluctuations) on the delocalization length.

from \ to	LH1	LH2	RC
LH1	20.0/N.A.	15.5/N.A.	15.8/30-50
LH2	7.7/3.3	10.0/N.A.	N.A
RC	8.1/8	N.A	N.A

TABLE I: Theoretical estimation/experimental evidence of inter-complex transfer times in picoseconds. N.A are not available data.

1.3 Dissipation

Excitation in chromophores might be dissipated by two main mechanisms. The first is fluorescence, where the electronic excited state has a finite lifetime on the nanosecond time-scale, due to its interaction with the electromagnetic

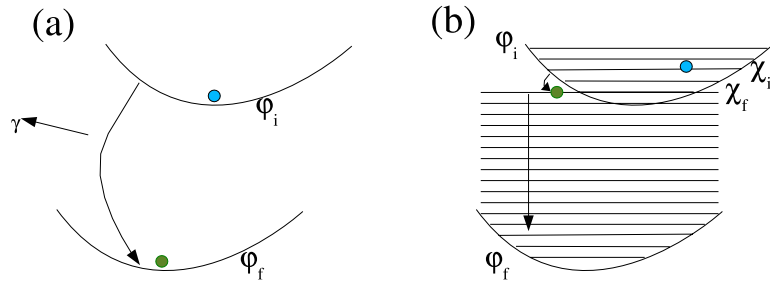


FIG. 4: Dissipation mechanisms. In (a), the electron de-excites due to its interaction with the quantized electromagnetic vacuum field through a fluorescent photon. In (b) internal conversion mechanism, where the vibrational levels overlap induces a transition between electronic excited and ground states. Dissipation overcomes when thermal equilibrium is reached in the vibrational manifold of electronic ground state.

vacuum [37]. The second is internal conversion, where the electronic energy is transferred to vibrational degrees of freedom.

Within the Born-Oppenheimer approximation, the molecular state Ψ , can be decomposed into purely electronic ϕ and (nuclear) vibrational χ states. The transition probability between initial state Ψ_i and final state Ψ_f , is proportional to $\langle \Psi_i | H | \Psi_f \rangle \propto \langle \chi_i | \chi_f \rangle$. Note that χ_i (χ_f) are vibrational levels in the ground (excited) electronic state manifold (see Fig.4). If the energy difference is small, and the overlap between vibrational levels of different electronic states is appreciable, the excitation can be transferred from the excited electronic state, to an excited vibrational level in the ground electronic state. This overlap increases with decreasing energy difference between electronic states. As higher electronic levels have smaller energy difference among their zero phonon lines, internal conversion process is more probable the higher energy electronic states have. Fluorescence and internal conversion between first excited singlet and ground electronic states, induce dissipation in a range of hundreds of picoseconds and a few nanoseconds. Numerical simulations are performed with a dissipation time including both fluorescence and internal conversion of $1/\gamma_D = 1$ ns, also used in [31].

1.4 Special pair (SP) ionization

From the LH1 complex excitation reaches the RC, specifically the special pair (SP) dimer. The excitation can be transferred back to its surrounding LH1, or initiate a chain of ionizations along the A branch, probably, due to a tyrosine residue strategically positioned instead of a phenylalanine present in the B branch [24]. Once the special pair is excited, it has been determined experimentally [10] that takes 3-4 ps for the special pair to ionize and produce a reduced bacteriopheophytin, H_A^- , in a reaction $SP^* \rightarrow SP^+ H_A^-$. This reaction initiates an electron hop, to a quinone Q_A in about 200 ps, and to a second quinone, Q_B if available. Initially, the ionized quinol Q_B^+ captures an intracytoplasmic proton and produces hydroxyquinol $Q_B H$, which after a second ionization that produces $Q_B H^+$ to form quinol $Q_B H_2$. After any SP ionization a neutrality reestablishment is required, provided by the cytochrome *cyt* charge carrier. After SP ionization, the cytochrome diffuses from the bc1 complex to a RC in order to replenish its neutrality $SP^+ \rightarrow SP$, within several microseconds [26]. The first electron transfer step $P^* \rightarrow P^+$ occurs in the RC within $t_+ = 3$ ps, used for quinol ($Q_B H_2$) production [17].

1.5 Quinone-quinol cycling

The RC cycling dynamics also involves undocking of $Q_B H_2$ from the RC due to lower affinity among RC and this new product. Quinol starts a migration to the bc1 complex where enables the ionization of the cytochrome *cyt* charge carrier, while a new quinone Q_B molecule docks into the RC. The time before quinol unbinds, and a new Q_B is available, has been reported within milliseconds [28] to highlight quinol removal as the rate limiting step [28] if compared to special pair reestablishment.

Even though it has been reported that excitation dynamics change as a function of the RCs state [3, 8], at a first glance the several orders of magnitude difference among the picosecond transfer, the nanosecond dissipation and the

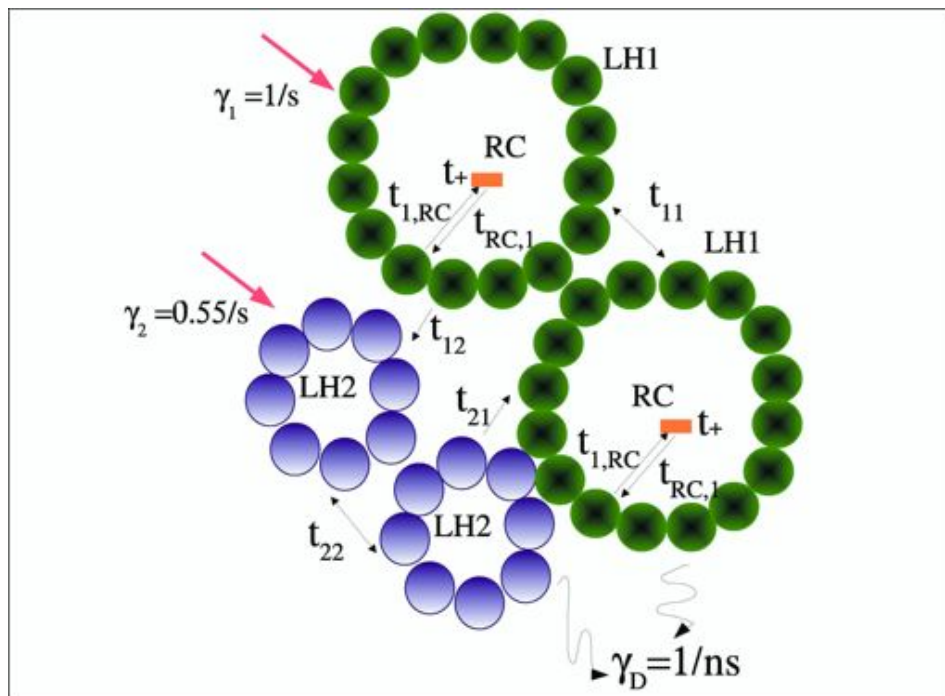


FIG. 5: Schematic of the biomolecular photosynthetic machinery in purple bacteria, together with relevant inter-complex mean transfer times t_{ij} , dissipation rate γ_D , and normalized light intensity rate $\gamma_{1(2)}$

millisecond RC cycling, seems to disregard important effects due to these mechanisms' interplay. However, the quinol-quinone dynamics leaves the RC unable to promote further quinol production and eventually enhances the influence of dissipation of a wandering excitation, evident when none RC is available and the unique fate of any excitation is to be dissipated.

Interestingly, the quinone-quinol mechanism has been well established and thought to be of priority on adaptations of bacteria, that seem to respond to its dynamics. For instance, an observed trend for membranes to form clusters of same complex type [33] seems to affect diffusion of quinones, enhanced when, due to higher mobility of LH1s, left void spaces help travel quinones to the periplasm. Negligible mobility of LH2s in their domains, would restrict metabolically active quinones to LH1 domains [35]. Easier diffusion of quinones, quinol and cytochromes promotes higher availability of charge carriers in RC domains under LLI conditions, increasing the rate at which RCs can cycle. The RC cycling dynamics and its connection to the membranes performance has been accounted in [5, 6] in a quantitative calculation to understand the effect of core clustering and stoichiometry variation in the RC supply or in the efficiency of the membranes from experimentally obtained Atomic Force Microscopy images, to be presented in this chapter.

2. Exciton kinetics

Figure 5 summarizes the relevant biomolecular complexes in purple bacteria *Rsp. Photometricum* [33], together with experimental– theoretical if the former are not available– timescales governing the excitation kinetics: absorption and transfer; and reaction center dynamics: quinol removal.

2.1 Model

The theoretical framework used to describe the excitation transfer must be built around the experimental (if available) and theoretical parameters just outlined. Remind that the thermalization process occurs faster than inter-complex energy transfer, and provides the support to rely in a classical hopping process, since phase information is lost well within the time frame implied by direct Coulomb coupling. Accordingly, we base our analysis on a classical random walk for excitation dynamics along the full vesicle, by considering a collective state with $N = N_2 + 2N_1$ sites –

resulting from N_2 LH2s, N_1 LH1s and hence N_1 RC complexes in the vesicle. The state vector $\vec{\rho} = (\rho_1, \rho_2, \dots, \rho_M)$ has in each element the probability of occupation of a collective state comprising several excitations. If a single excitation is allowed in each complex, both excited and ground states of any complex should be accounted and the state space size is $M = \underbrace{2 \times 2 \times 2 \dots}_N = 2^N$. On the other hand, if only one excitation that wanders in the whole network of complexes is allowed, a site basis can be used where each element of the state vector gives the probability of residence in the respective complex, and reduces the state vector size to $M = N$. In either case the state vector time evolution obeys a master equation

$$\partial_t \rho_i(t) = \sum_{j=1}^M G_{i,j} \rho_j(t). \quad (16)$$

where $G_{i,j}$ is the transition rate from a collective state or site i – whether many or a single excitation are accounted, respectively – to another collective state or site j . Since the transfer rates do not depend on time, this yields a formal solution $\vec{\rho}(t) = e^{\tilde{G}t} \vec{\rho}(0)$. However, the required framework depends on exciton abundance within the whole chromatophore at the regime of interest.

For instance, purple bacteria ecosystem concerns several meters depths, and should be reminded as a low light intensity environment. Within a typical range of 10-100 W/m² and a commonly sized chromatophore having ≈ 400 LH complexes, eq.(2) leads to an absorption rate $\gamma_A \approx 100-1000 \text{ s}^{-1}$, which compared with the dissipation mechanisms (rates of $\approx 10^9 \text{ s}^{-1}$) imply that an absorption event occurs and then the excitation will be trapped by a RC or become dissipated within a nanosecond, and other excitation will visit the membrane not before some milliseconds have elapsed. However, it is important to remind the nature of thermal light where the possibility of having bunched small or long inter-photon times is greater than evenly spread, with greater deviations from poissonian statistics the grater its mean intensity is. Therefore, regardless of such deviations, under the biological light intensity conditions, the event of two excitations present simultaneously along the membrane will rarely occur and a single excitation model is accurate.

2.2 Small architectures

Small absorption rates lead to single excitation dynamics in the whole membrane, reducing the size of $\vec{\rho}(t)$ to the total number of sites N . The probability to have one excitation at a given complex initially, is proportional to its absorption cross section, and can be written as $\vec{\rho}(0) = \frac{1}{\gamma_A} (\underbrace{\gamma_1, \dots}_{N_1}, \underbrace{\gamma_2, \dots}_{N_2}, \underbrace{0, \dots}_{N_1})$, where subsets correspond to the N_1

LH1s, the N_2 LH2s and the N_1 RCs respectively.

2.2.1 Complexes arrangement: architecture

To gain physical insight on the global behavior of the harvesting membrane, our interest lies in the probability to have an excitation at a given complex kind $k \in \text{LH1, LH2 or RC}$, namely \hat{p}_k , given that at least one excitation resides in the network:

$$\hat{p}_k(t) = \frac{\rho_k(t)}{\sum_{i=1}^N \rho_i(t)}. \quad (17)$$

The effects that network architecture might have on the model's dynamics, are studied with different arrangements of complexes in small model networks, focusing on architectures which have the same amount of LH1, LH2 and RCs as shown in the top panel of Fig.6(a), (b) and (c). The bottom panel Fig.6 (d)-(e)-(f) shows that \hat{p}_k values for RC, LH1 and LH2 complexes, respectively. First, it is important to notice that excitations trend is to stay within LH1 complexes, and not in the RC. Fig.6(d) shows that the highest RC population is obtained in configuration (c), followed by configuration (a) and (b) whose ordering relies in the connectedness of LH1s to antenna complexes. Clustering of LH1s will limit the number of links to LH2 complexes, and reduce the probability of RC ionization. For completeness, the probability of occupation in LH1 and LH2 complexes (Figs.6(e) and (f), respectively), shows that increased RC occupation benefits from population imbalance between LH1 enhancement and LH2 reduction. As connections among antenna complexes become more favored, the probability of finding an excitation on antenna complexes will become

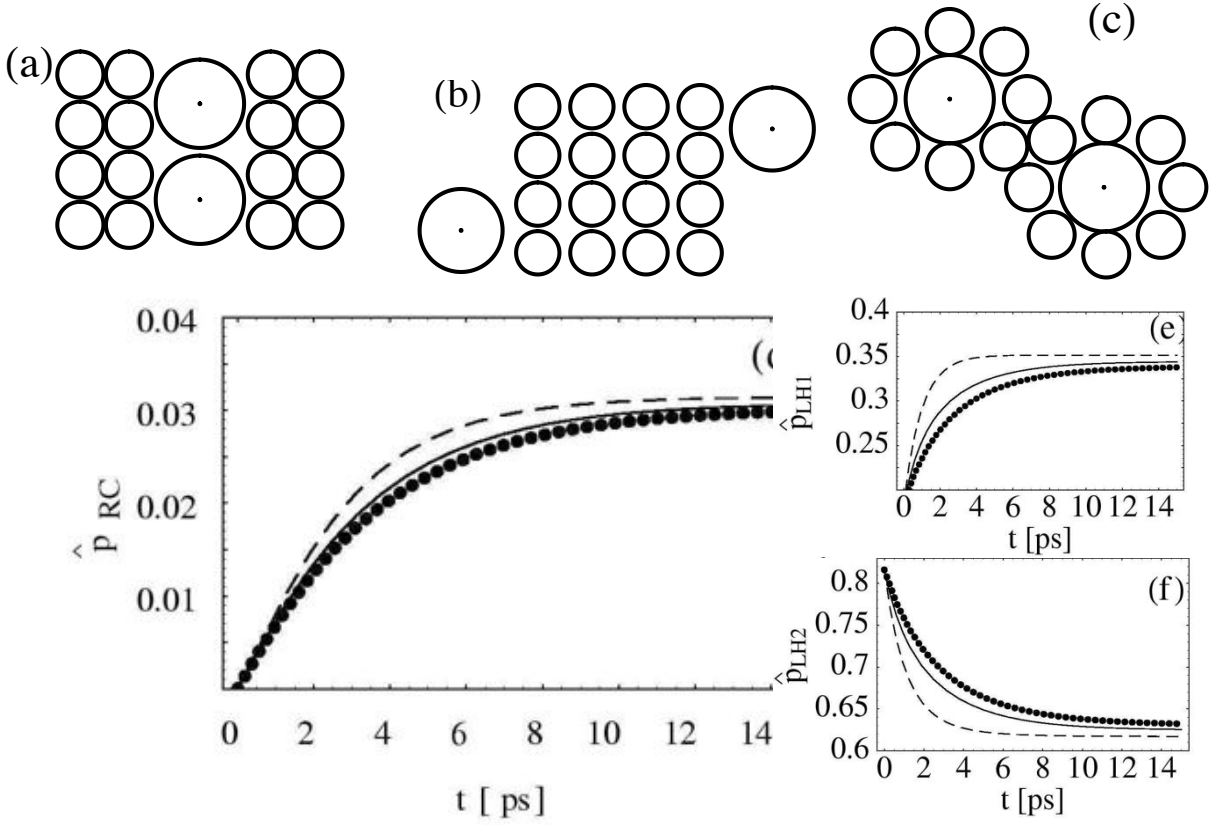


FIG. 6: Top panel: Three example small network architectures. The bottom panel shows the normalized probabilities for finding an excitation at an RC (see (d)), an LH1 (see (e)), or an LH2 (see (f)). In panels (d)-(f), we represent these architectures as follows: (a) is a continuous line; (b) is a dotted line; (c) is a dashed line.

smaller, while the probability of finding excitations in RCs is enhanced. This preliminary result, illustrates that if the apparent requirement to funnel excitations down to RCs in bacterium were of primary importance, the greatest connectedness of LH1-LH2 complexes should occur in nature as a consequence of millions of years evolution. However, as will be presented, the real trend to form LH1 clusters, reduces its connectedness to antenna LH2 complexes and somehow pinpoints other mechanisms as the rulers of harvesting membranes conformation and architecture.

2.2.2 Relative amount of complexes: Stoichiometry

We can also address with use of small architectures the effect of variation in the relative amount of LH1/LH2 complexes, able to change the population of the available states. Fig.7 shows small networks of LH-RC nodes, where the relative amount of LH2 and LH1 complexes quantified by stoichiometry $s = N_2/N_1$ is varied, in order to study the exciton dynamics. In Fig.8(a) the population ratio at stationary state of LHs demonstrate that as stoichiometry s becomes greater, the population of LH1s, becomes smaller, since their amount is reduced. It is apparent that RC population is quite small, and although their abundance increases the exciton trend to be found in any RC (Fig.8(b)), generally, excitations will be found in harvesting complexes. The population of LHs should be dependent on the ratio of complexes type. As verified in Fig.8(b), RCs have almost no population, and for the discussion below, they will not be taken into account. Populations can be written as:

$$\hat{p}_1(t \rightarrow \infty) = f_1(s) \frac{N_1}{N_1 + N_2} = \frac{f_1(s)}{1 + s} \quad (18)$$

$$\hat{p}_2(t \rightarrow \infty) = f_2(s) \frac{N_2}{N_1 + N_2} = \frac{s f_2(s)}{1 + s} \quad (19)$$

where the dependence on the amount of complexes is made explicit with the ratio $\frac{N_k}{N_1 + N_2}$, and where $f_1(s)$ and $f_2(s)$ are enhancement factors. This factor provides information on how the population on individual complexes changes,

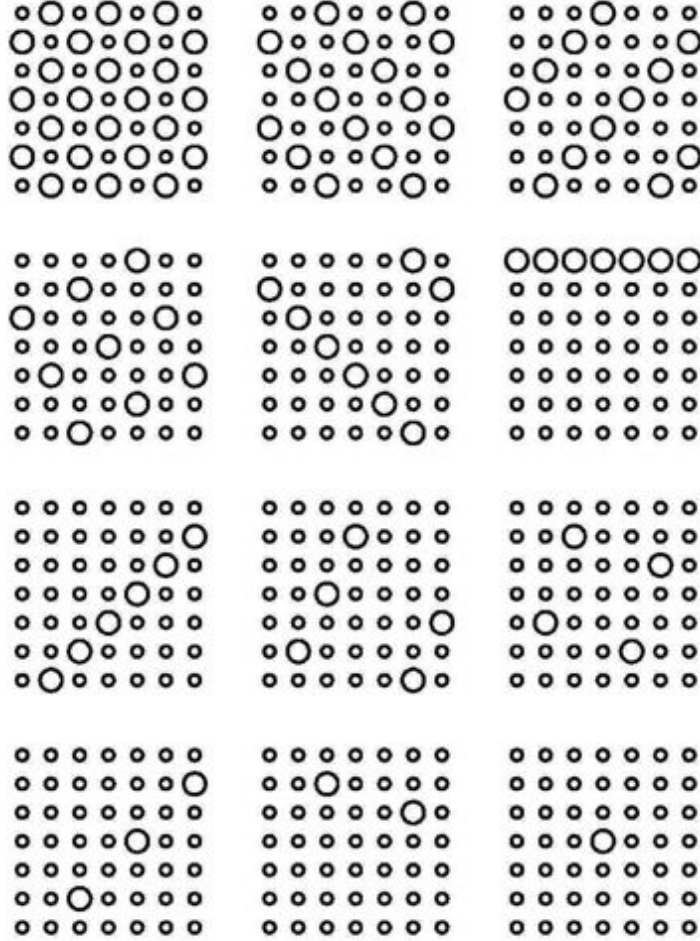


FIG. 7: Networks with different stoichiometries, from left to right, top to bottom, $s=\{1.04, 2.06, 3.08, 4.44, 5.125, 6, 7.16, 8.8, 11.25, 15.33, 23.5, 48\}$, and equal number of harvesting complexes.

beyond the features arising from their relative abundance. With use of eqs.(18-19), $f_1(s)$ and $f_2(s)$ can be numerically calculated provided that $\hat{p}_k(t \rightarrow \infty)$ can be known from the master equation, while s is a parameter given for each network. The results for enhancement factors are presented in Fig.8(c). The enhancement factor $f_2(s)$ for LH2 seems to saturate at values below one, as a consequence of the trend of excitations to remain in LH1s. This means that increasing further the number of LH2s will not enhance further the individual LH2 populations. On the other hand $f_1(s)$ has a broader range, and increases with s . This result reflects the fact that population of individual LH1s will become greater as more LH2 complexes surround a given LH1. An unconventional architecture (third column, second row in Fig.7) has an outermost line of LH1 complexes, whose connectedness to LH2s is compromised. In all the results in Fig. 8 (sixth point), this architecture does not follow the trends just pointed out, as LH1 and RC population, and enhancement factors, are clearly reduced. The population of LH1 complexes depends on their neighborhood and connectedness. Whenever connectedness of LH1 complexes is lowered, their population will also be reduced. Hence, deviations from populations trend with variation of stoichiometry, are a consequence of different degrees of connectedness of LH1s.

Up to this point, the master equation approach has helped us understand generally the effect of stoichiometry and architecture in small networks. Two conclusions can be made:

1. Connectedness of LH2 complexes to LH1s, facilitates transfer to RCs
2. The relative amount of LH2/LH1 complexes, namely, stoichiometry $s = N_2/N_1$, when augmented, induces smaller population on LH1-RC complexes. On the other hand, smaller s tends to increase the connectedness of

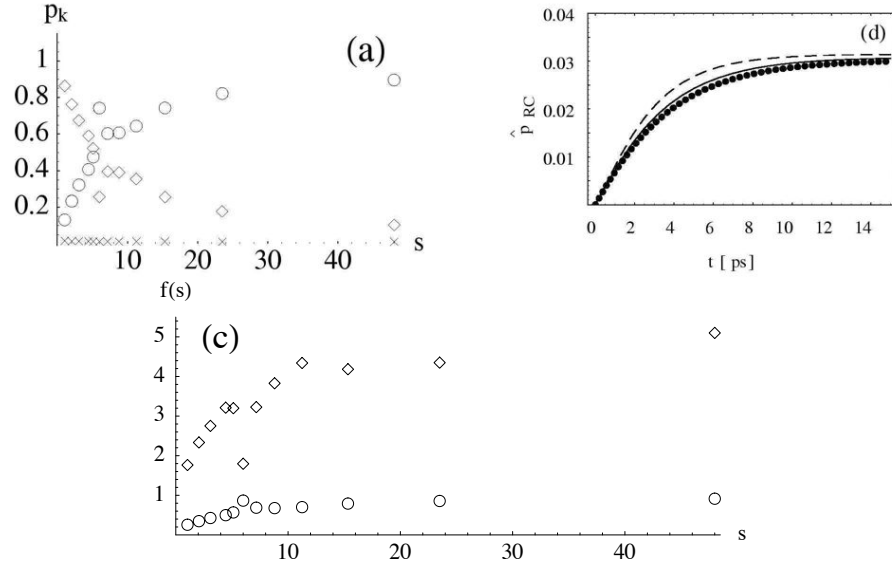


FIG. 8: In (a) stationary state populations for LH2s (circles), LH1s (diamonds) and RCs (crosses), as a function of the stoichiometry of membranes presented in Fig.7. In (b) a zoom of RC populations is made, and in (c) the enhancement factors $f_1(s)$ (diamonds) and $f_2(s)$ (circles) are presented.

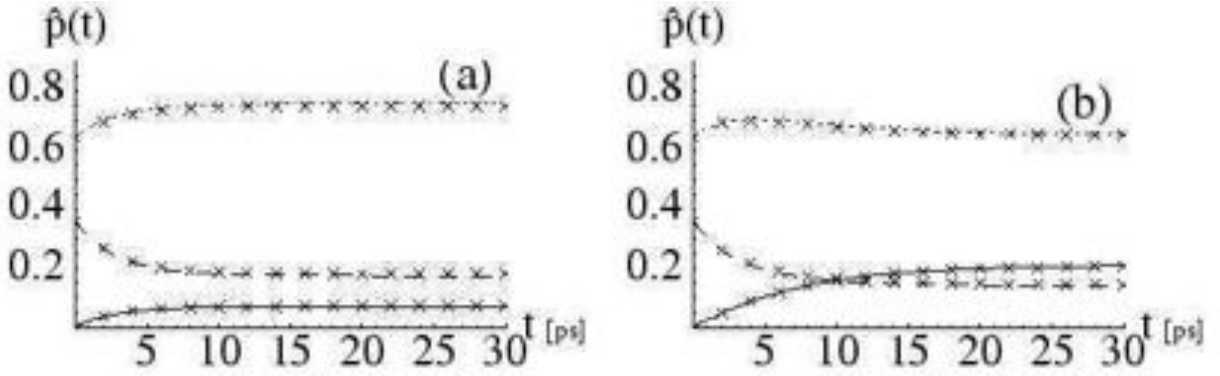


FIG. 9: Normalized probabilities \hat{p}_k for finding the excitation at an LH2 (dashed), LH1 (dotted) or at an RC (continuous), for (a) $t_+ = 3\text{ps}$, and (b) $t_+ \rightarrow \infty$. Crosses are the results from the Monte Carlo simulation.

LH1s to LH2s and hence, the population of individual LH1 complexes.

2.2.3 Special pair ionization

Another basic process involved in the solar energy conversion is the ionization of the special pair in the RC, and eventual quinol $Q_B H_2$ formation. Remind that once quinol is formed, the special pair is unable to use further incoming excitations before quinol undocks and a new quinone replaces it. Even though the RC neutrality-diffusion process is propelled by complicated dynamics and involved mechanisms, in an easy approach, let us assume that the RC dynamics will proceed through a dichotomic process of "open" and "closed" RC states. In the open state, special pair oxidation is possible, while when closed, special pair oxidation to form quinol never happens, hence $t_+ \rightarrow \infty$

The effect of open and closed RC states changes the exciton kinetics. We start with a minimal configuration corresponding to a basic photosynthetic unit: one LH2, one LH1 and its RC. Figure 9(a) shows that if the RC is open, excitations will mostly be found in the LH1 complex, followed by occurrences at the LH2 and lastly at the RC. On the other hand, Figure 9(b) shows clearly the different excitation kinetics which arise when the RC is initially unable to start the electron transfer $P^* \rightarrow P^+$, and then after $\approx 15\text{ps}$ the RC population becomes greater with respect to the LH2's. This confirms that a faithful description of the actual photosynthesis mechanism, even at the level of the minimal

unit, must resort into RC cycling, given that its effects are by no means negligible. Moreover, comparison among Figs.6(d) and 9 also presents a feature that is usually undermined when small architectures are used to straightforwardly interpret its results as truth for greater, real biological vesicles. Energy funneling becomes smaller with the number of antenna LH2 complexes, thereby, in architectures with many harvesting antenna complexes, excitation will find it more difficult to arrive to any of the relatively spread RCs. Besides, although LH2→LH1 transfer rate is five-fold the back-transfer rate, the amount of smaller sized LH2s neighboring a given LH1 will increase the net back-transfer rate due to site availability. Hence, the funneling concept might be valid for small networks [17, 31], however, in natural scenarios involving entire chromatophores with many complexes, energy funneling might not be priority due to increased number of available states, provided from all LH2s surrounding a core complex, and globally, from the relative low RC abundance within a real vesicle.

It is important to mention that results for master equation calculations require several minutes in a standard computer to yield the results shown in Fig.8, and that these networks have an amount of nodes an order of magnitude smaller than the actual chromatophore vesicles. Dynamics concerning the RC cycling have not been described yet, fact that would increase further the dimension of possible membrane's states. To circumvent this problem, further analysis will proceed from *stochastic simulations*, and observables will be obtained from ensemble averages.

2.3 Full vesicles

A real vesicle involves several hundreds of harvesting complexes. Given the large state-space needed to describe such amount of complexes and our interest to inquire on a variety of incoming light statistics in the sections ahead, our subsequent model analysis will be based on a discrete-time random walk for excitation hopping between neighboring complexes.

Simulation algorithm.

In particular, we use a Monte Carlo method to simulate the events of excitation transfer, the photon absorption, the dissipation, and the RC electron transfer. We have checked that our Monte Carlo simulations accurately reproduce the results of the population-based calculations described above, as can be seen from Figs.9(a) and (b). The Monte Carlo simulations proceed as follows. In general, any distribution of light might be used with the restriction of having a mean inter-photon time of γ_A^{-1} from eq.(2). Accordingly, a first photon is captured by the membrane and the time for the next absorption is set by inverting the cumulative distribution function from a [0,1] uniformly distributed (Unit Uniformly Distributed, UUD) random number. This inverting procedure is used for any transfer, dissipation or quinol removal event as well. The chosen absorbing complex is randomly selected first among LH1 or LH2 by a second UUD number compared to the probability of absorption in such complex kind, say $N_{1(2)}\gamma_{1(2)}/\gamma_A$ for LH1 (LH2), and a third UUD random number to specifically select any of the given complexes, with probability $1/N_{1(2)}$. Once the excitation is within a given complex, the conditional master equation given that full knowledge of the excitation residing in site i , only involves transfers outside such site, say $\partial_t \rho_i = -(\sum_j 1/t_{i,j} + \gamma_D)\rho_i$, whose solution is straightforward to provide the survival probability and its inverse, of use to choose the time t^* for the next event according to eq.(16) from a UUD number r : $-\log r / (\sum_j 1/t_{i,j} + \gamma_D) = t^*$. Once t^* is found, a particular event is chosen: transfer to a given neighboring complex j with probability $(1/t_{i,j}) / (\sum_j 1/t_{i,j} + \gamma_D)$ or dissipation with probability $\gamma_D / (\sum_j 1/t_{i,j} + \gamma_D)$, which are assigned a proportional segment within [0,1] and compared with another UUD number to pinpoint the particular event. If the chosen event is a transfer step, then the excitation jumps to the chosen complex and the transfer-dissipation algorithm starts again. If dissipation occurs, the absorption algorithm is called to initiate a new excitation history. In a RC, the channel of quinol ionization is present with a rate $1/t_+$ in an event that if chosen, produces the same effect as dissipation. Nonetheless, the number of excitations that become SP ionizations are counted on each RC, such that when two excitations ionize a given RC and produce quinol, it becomes closed by temporally setting $1/t_+ = 0$ at such RC. Quinol unbinding will set "open" the RC, not before the RC-cycling time with mean τ , has elapsed, chosen according to a poissonian distribution. The algorithm can be summarized as follows:

1. Create the network: Obtain coordinates and type of LHs, and label complexes, for instance, by solely numerating them along its type, say complex 132 is of type 2 (we use 1 for LH1, 2 for LH2 and 3 for RC). Choose the j neighbors of complex i according to a maximum center to center distance less than $r_1 + r_2 + \delta$, $r_2 + r_2 + \delta$ and $r_1 + r_1 + \delta$ for respective complexes. We use $\delta = 20\text{\AA}$, chosen such that only nearest neighbors are accounted and

further increase of δ makes no difference on the amount of nearest neighbor connections, although further increase may include non-physical next to near-neighbors. In practice, the network creation was done by three arrays, one, say $neigh(i, j)$ with size $M \times S$, with M complexes as described above, and S as the maximum number of neighboring complexes among all the sites, hence requiring several attempts to be determined. Minimally $j \leq 1$ for an LH2, concerning the dissipation channel, $j \leq 2$ for LH1 including both dissipation and transfer to its RC, and $j \leq 3$ for a RC accounting on dissipation, RC ionization and transfer to its surrounding LH1. The other arrays are built, say $size(i)$, with M positions, that keep on each the number of neighbors of the respective i labelled complex, and $rates(i, j)$ where at each position the inter-complex rate $i \rightarrow j$ is saved. For instance, $rates(i, 1)$ of any RC will be the ionization rate $1/t_+$.

2. Send photons to the network: On a time $t^* = -\log(r)/\gamma_A$ according to eq.(2), with r being an UUD number. Choose an LH2 or an LH1, according to the probability of absorption from the cross section of complex type $N_{1(2)}\gamma_{1(2)}/\gamma_A$. Add one excitation to the network, say $n = n + 1$, and assign the initial position $pos(n) = i$ of the excitation according to another UUD that selects an specific labelled i complex. Remind that n is bounded by the maximum amount of excitations allowed to be at the same time within the membrane, usually being one.
3. If the i th complex is excited, the construction of the above mentioned arrays make the cycle of excitation dynamics straightforward since the network is created only once, and dynamics only require to save the complex i where the excitation is, and then go through cycles of size $size(n, i)$ to acknowledge the stochastically generated next time for a given event. Excitation can be transferred to the available neighbors, become dissipated or a RC ionization event. Order all times for next events in order to know which will be the next in the array, say $listimes(p)$ with $p \leq n$, where $t_{\min} = listemp(1)$. In parallel, update an organized array that saves the next process with the number of the neighbor to which hopping occurs, or say a negative number for RC ionization and another negative number for dissipation.
4. Jump to next event: By cycling over the n present excitations, increase time up to the next event t_{\min} . If RC cycling is accounted, check which time among t_{min} and the next opening RC time t_{RC} (its algorithm is to be discussed in the following) is the closest, and jump to it.
5. Change state of excitations or that of RCs: Update the current site of the excitation n , or whether it becomes a dissipation or a RC ionization. If the latter process occurs, keep in an array, say $rcstate(k)$ whose size equals the total amount of RCs, the number of excitations that have become ionizations from the last time the k th RC was opened. If $rcstate(k) = 2$ then the k th RC is closed by redefinition of $rate(i, 1) = 0$ and a poissonian stochastically generated opening time with mean τ is generated. This time interval is kept in an array $rcimes(k)$. Now, introduce this time interval into an ascending ordered list among all closed RCs opening times such that the minimum t_{RC} is obtained. If $t_{RC} < t_{\min}$ then jump to that time and open the k th RC by letting $rcstate(k) = 0$ and $rates(i, 1) = 1/t_+$.
6. Look which is minimum among t^* , t_{RC} and t_{\min} and jump to steps 2 or 4 according to whether $t^* < (t_{RC}, t_{\min})$ or $(t_{RC}, t_{\min}) < t^*$, respectively.
7. If the maximum amount of excitations chosen from the initialization, have been sent to the membrane, finish all processes and write external files.

The language used to program this algorithm was FORTRAN77, to point out that these calculations do not require any high-level language.

Excitation dynamics trends in many node-complexes networks.

In order to understand at a qualitative degree the excitation dynamics trends involved in full network chromatophores, a few toy architectures have been studied, shown in Fig.10. In this preliminary study it is of interest to understand the excitation kinetics in complete chromatophores. In particular, it is useful to understand if any important feature arises according to nature's found tendency of forming clusters of the same complex type. In AFM images [34] it has been found that there is an apparent trend to form clusters of LH1 complexes with simultaneous formation of LH2 para-crystalline domains. The reason that has been argued for this trend [34] involves the RC cycling dynamics and can be explained as follows.

The charge carrier quinone-quinol require diffusing through the intracytoplasmic membrane within the void spaces left among harvesting complexes, in order to reach the bc1 complex and complete the electric charge cycle with

cytochrome that however, diffuses through the periplasm as schematically shown in Fig.2. The closeness among LH2 complexes in these para-crystalline domains restricts the void spaces required for diffusion of quinone-quinol to the LH1 domains, where charge separation is taking place. Then, such aggregation indeed helps to improve the time it takes to quinone perform the whole RC-bc1-RC cycle, by restricting its presence to RC domains. However, an advantage concerning excitation dynamics has been heuristically proposed, where the path an excitation has to travel to reach an open RC once it encounters a closed RC is reduced due to LH1 clustering. In this section we investigate this latter possibility from a more quantitative point of view and address the former in the next section.

In order to understand exciton kinetics, for instance, let us fix our attention on the probability of a RC ionization when excitations start in a given LH2 on the configurations shown in Fig.10. To that end, let us introduce first the number n_{RCij} of excitations that are absorbed at site i and become ionization of the special pair at a given RC, labeled j . Also let \hat{r}_{ij} be the unitary vector pointing in the direction from LH2 site i to RC site j . As an analogous to a force field, let vector field \mathbf{v} correspond to a weighted sum of the directions on which RC ionizations occur, starting for a given LH2 complex

$$\mathbf{v}_i = \frac{\sum_j n_{RCij} \hat{r}_{ij}}{\sqrt{\sum_j n_{RCij}^2}}. \quad (20)$$

of help as a purely numerical calculation of graphical interpretation. The normalization gives a basis to compare only the directions for RC ionizations independent whether excitations are dissipated or not. Note that \hat{r}_{ij} has both positive and negative signs, hence the vector \mathbf{v}_i will have greater magnitude as RC ionizations occur more frequently at a given direction, or less magnitude as ionizations occur in more spread out directions.

Several features can be understood from this vector field. Figure 10 shows the vector fields attracted to the LH1 most abundant regions. The arrows illustrate the favored statistical direction in which excitations will become RC ionization, and they do not imply that an excitation will deterministically move in that direction if it were absorbed in such place. Firstly, in all cases, a tendency to point on clustered LH1s stands from distant LH2 complexes, a fact that emphasizes the very rapid transfer rates that lead to excitation's rapid global membrane sampling. Secondly, it is evident that better excitation attractors are made with increasing the core centers cluster size, easily observed in the top panel. Hence, according to this result one may naively state that a funneling effect is apparent and strongly dependent on cluster size. However, on the middle panel, it can be seen that this funneling effect is vanishingly small at sites where some degree of symmetry is present concerning the distribution of neighboring RCs, even though if these latter display some clustering degree. Third, a trend is displayed where the spreading of the flux becomes smaller with a lesser amount of RCs. However it is important to be aware that in more detail and in a general fashion, one also sees that even the LH2s closest to a given RC, "feel" the presence of further RCs. This implies that a significant amount of excitations that reach LH2 complexes neighboring a given LH1, will better prefer hopping to neighboring LH2 complexes to eventually reach a distant RC: no "funneling", as usually understood.

In a more realistic situation, the clustering of LH1 complexes is just a trend, and in average any cluster is formed by a few 3-4 core complexes in HLI situations and somehow less for LLI membranes as shown in Fig.11, where empirical architectures are presented in complete accordance with experimental data, taken from Ref.[33]. Along these figures, the vector field calculated for the HLI and LLI empirical membranes is made, to highlight no clear trend of excitations to be transferred immediately to neighboring LH1 complexes, and disregard a funneling LH2→LH1 as the unique direction of excitation flux when many complexes are accounted.

In detail, from the reasons just provided, in Fig.11(a) it is apparent that in HLI membranes, individual LH1 complexes are not efficient attractors of excitations. Here, not even the LH2s closest to a core center complex are notably attracted to such cores. On the other hand, a more uniform flux seems to be shared on clusters of LH2s in the LLI membrane (Fig.11(b)), that points to locations where more core centers are displayed. Hence, it is more evident the directionality of the flux to the most LH1 abundant locations that gives a statistical preference to ionize the closest RCs due their low global abundance in LLI membranes. The greater amount of LH1 complexes in the HLI membrane induces no significant preference for excitations to hop to the closest lying RCs and provides evidence that the excitation process proceeds without a clear funneling effect. If a single excitation can become an ionization in a single RC, the flux is clear, but if there are many and spread, the flux becomes random, as would be expected from any random walk. In summary, these results allow a mental picture of the excitation transfer process: Excitations become absorbed and start wandering along the membrane in a random walk regardless of a funneling effect, up to the moment where they reach a RC and become ionized, in a process where statistical preference is present in LLI membranes due to the reduced amount of RC, and presenting more clearly the random wandering on HLI due to higher spread out possibilities of ionization. This fact can also be quantitatively investigated.

Suppose that a given LH1 is surrounded by a few LH2 complexes. If an excitation is absorbed into one of these

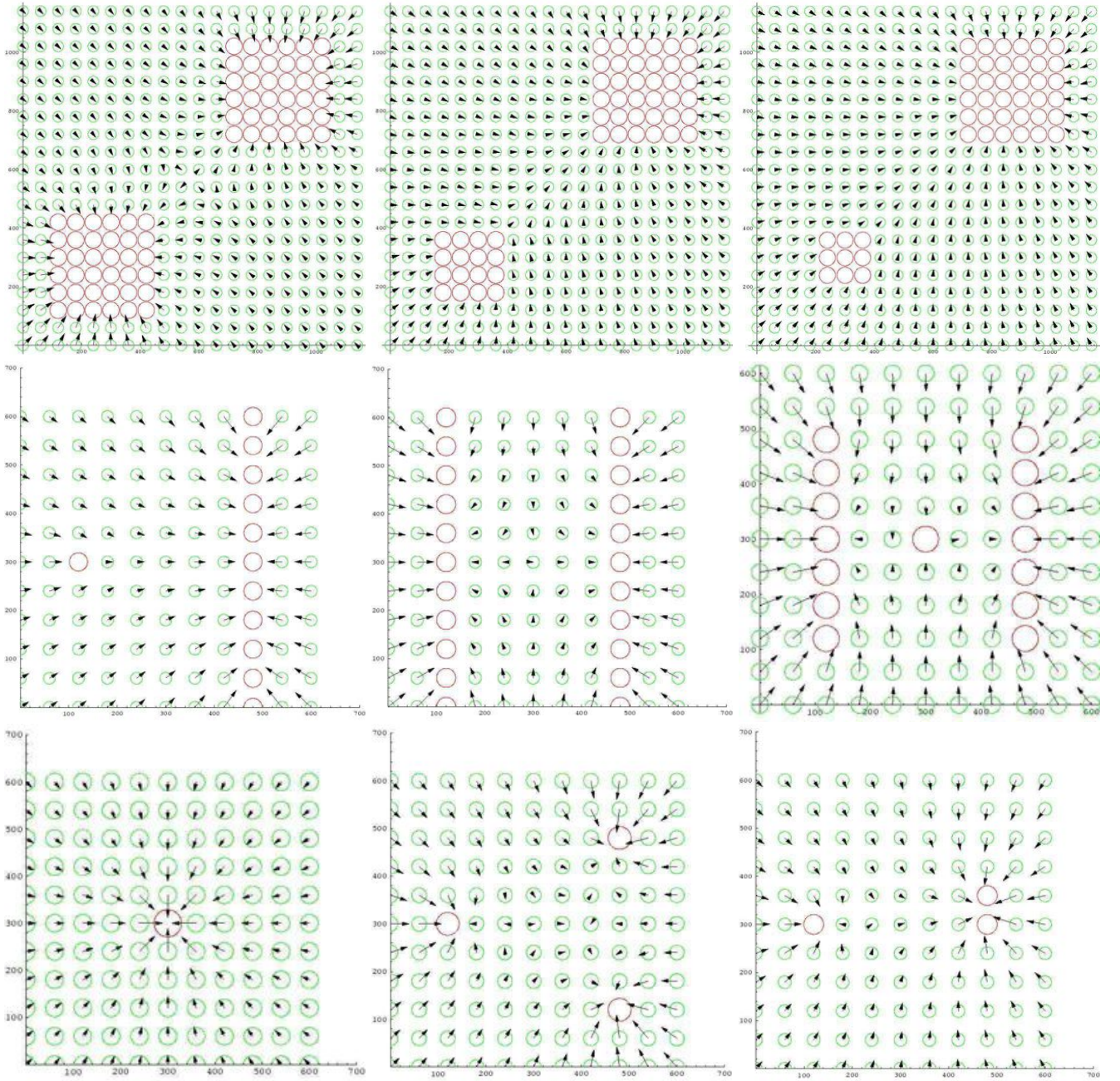


FIG. 10: Vector field \mathbf{v} for different configurations, where the effect of core centers clustering is investigated (100000 runs starting in each site).

neighboring LH2s, it will have a survival probability decaying with rate $1/t_{21} + n/t_{22}$ where n would be 3-4 corresponding to the number of LH2s neighboring such absorbing LH2. Given the presented transfer times (remind $t_{21} = 3.3\text{ps}$ and $t_{22} = 10\text{ps}$) both terms in the survival decay rate become almost equal for $n = 3$, and hence no preference will occur on the excitation to be transferred to the closest LH1. If LH2 \rightarrow LH1 transfer would actually happen, the same exercise can be done for the survival probability within the LH1 complex, decaying with a rate $m/t_{12} + 1/t_{1,RC}$ (remind $t_{12} = 15.5\text{ps}$ and $t_{1,RC} \approx 30\text{ps}$) which assuming a single surrounding LH2 complex ($m = 1$) would give a preference for excitations to return to antenna complexes. Hence, if the availability of neighbors is accounted, the funneling LH2 \rightarrow LH1 is lost, which along the enhanced back-transfer rate LH1 \rightarrow LH2 as compared to LH1 \rightarrow RC, provides the basis for understanding complete chromatophores as networks where actual performance depends upon the RC availability, since the event of ionization only depends on the probability to get to RC sites having no preference

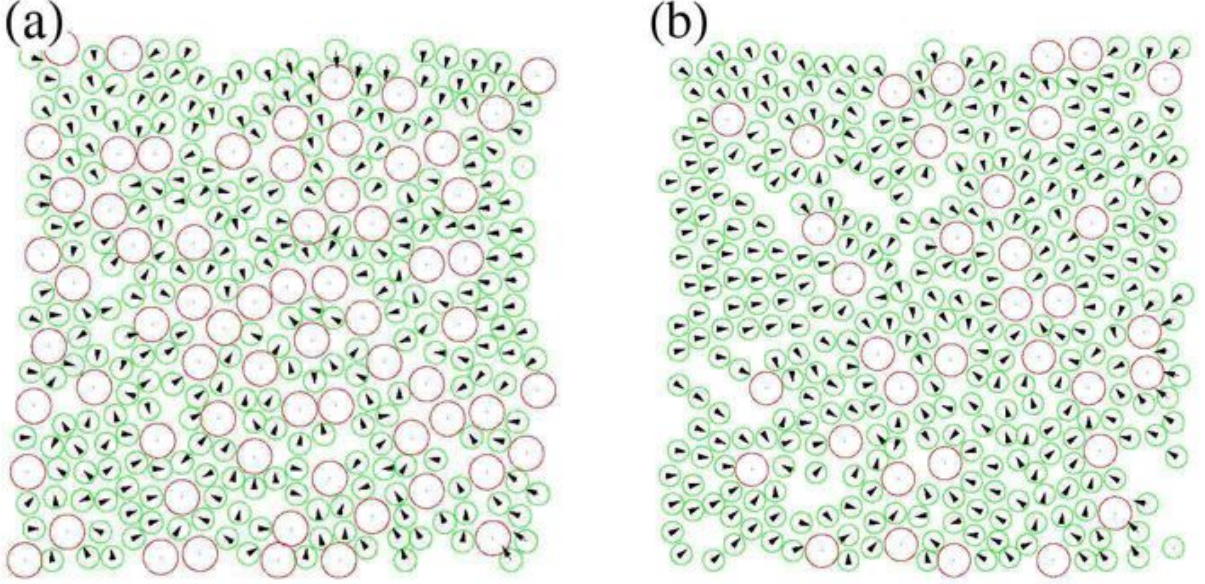


FIG. 11: Vector field \mathbf{v} for HLI (a) and LLI (b) membranes (100000 runs each site).

to be visited within the network. Excitations sample great portions of the whole membrane in its hopping, hence become able to reach RCs far away from the absorption sites before dissipation overcomes.

Dissipation itself also provides interesting features. The dissipation d_i measures the probability for excitations to dissipate at site i from the the total amount of excitations being absorbed in the membrane n_A :

$$d_i = \frac{n_{D_i}}{n_A} \quad (21)$$

that has an straightforward relation with the global efficiency η of the membrane, that accounts on the probability of any excitation to be used as an SP ionization. Given that excitations can only become RC ionizations or be dissipated, the sum over all complexes of dissipation probability will give the probability of any excitation to be dissipated, hence

$$\eta = 1 - \sum_i d_i \quad (22)$$

Figure 12 shows the dissipation on the membranes shinned with the respective illumination rate of their growth (LLI 10 W/m² and HLI 100 W/m²). Figure 12(a) shows that the LLI membrane has highly dissipative clusters of LH2s, in contrast to the uniform dissipation in the HLI membrane (see Fig.12(b)).

This result addresses distinct features probably connected with the own requirements for bacteria when different light intensity is used during growth. Under LLI, bacterium might require use of all the available solar energy to promote its metabolism. In the numerical simulations (as expected from nature), the dissipation rate is set equal on any site, and therefore dissipation is only dependent on the probability for an excitation to be in a given complex. If more dissipation is found in some regions, it can there be supposed that excitations remain more time at such domains. Hence the tendency for excitations to dissipate implies they reside longer in LH2 complex domains and justify the view of LH2 clusters as excitation reservoirs. Although RC cycling has not been accounted yet, a given history might include an event where the excitation reaches closed clustered RCs and then jumps back to these LH2 domains waiting before the RCs become available again. On the other hand, HLI membranes display an evenly distributed dissipation. For instance, at HLI not all excitations might be required and dissipation can be used as a photo-protective mechanism. In this case, if dissipation were highly concentrated, vibrational recombination would overheat such highly dissipating domains.

Beyond these local details, an analysis regarding average values of dissipation D_k and residence p_{R_k} probabilities on a complex type k ($k = 1, 2$ are respectively LH1, LH2 complexes) better supports the view of a completely random excitation hopping process. Table II shows the numerical results of p_{R_k} , that concerns the probability to find an excitation in a given complex type and is calculated from the sum of the residence times of excitations at a given

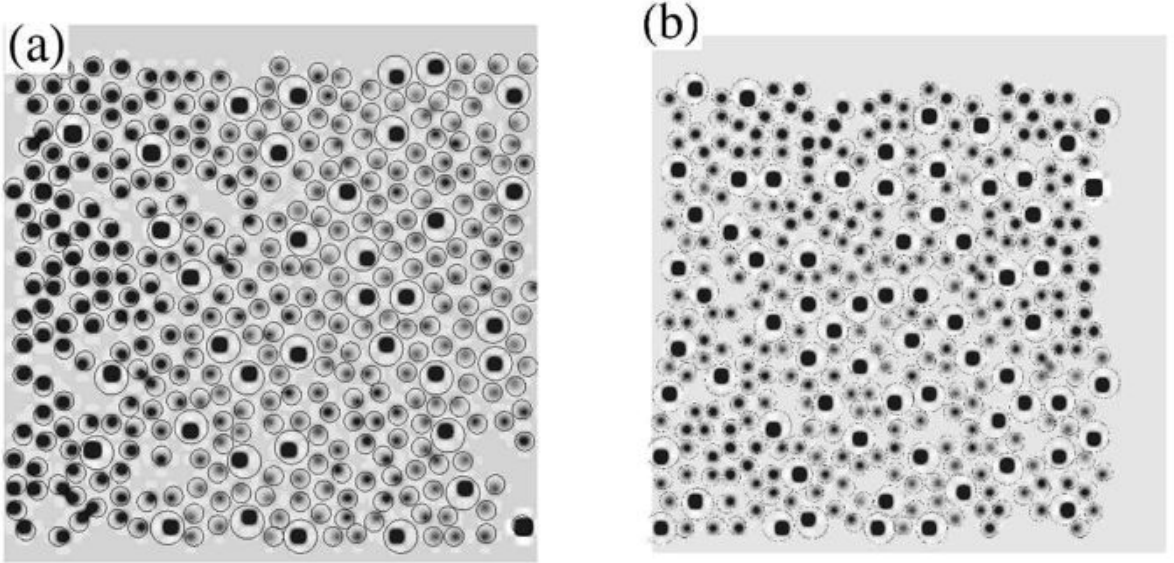


FIG. 12: Contour plots for dissipation in LLI (a) and HLI (b) membranes. Greater contrast means higher values for dissipation. The simulation is shown after 10^6 excitations were absorbed by the membrane with rate γ_A .

complex type. It is straightforward to see that p_{R_k} is closely related to the probability of dissipation at such complex type, therefore, dissipation can correctly measure where excitations are to be found in general. The randomness of excitation dynamics is illustrated by realizing that dissipation in a given complex type depends primarily on its relative abundance, since $\frac{D_k}{D_j} \approx \frac{N_k}{N_j}$, and justifies that apart from LH2 clusters local variations, in the mean, all sites behave equivalently, and no dynamical feature arises to set a difference among LH1s and LH2s able to argue on the stoichiometry adaptation experimentally found. Lastly, as expected from the dynamical equivalence of sites, along the result obtained with toy architectures of varying stoichiometry where RC population heavily rose due their abundance but relatively invariant to arrangement, the probability to reach a RC solely depends on its abundance, and therefore the global efficiency η is greater in HLI membranes.

Membrane	p_{R_2}	p_{R_1}	D_2	D_1	$\frac{D_2}{D_1}$	$s = \frac{N_2}{N_1}$	$\eta = 1 - \frac{n_D}{n_A}$
LLI	0.72	0.25	0.74	0.26	9.13	9.13	0.86
HLI	0.50	0.46	0.52	0.48	3.88	3.92	0.91

TABLE II: Dissipation D_k , residence probability p_{R_k} , on $k = \{1, 2\}$ corresponding to N_1 LH1 and N_2 LH2 complexes respectively. Stoichiometry s and efficiency η are also shown.

Hence, for the present discussion, the most important finding from these numerical simulations is that the adaptation of purple bacteria does *not* lie in the single excitation kinetics. In particular, LLI membranes are seen to reduce their efficiency globally at the point where photons are becoming scarcer – hence the answer to adaptation must lie in some more fundamental trade-off (as we will later show explicitly). Due to the dissimilar timescales between millisecond absorption from eq.(2) and nanosecond dissipation, multiple excitation dynamics are also unlikely to occur within a membrane. However, multiple excitation dynamics cannot be regarded *a priori* not to be a reason for purple bacteria adaptation. A numerical study in Ref.[5] involving blockade in which two excitations can not occupy the same site and annihilation, where two excitations annihilate due to vibrational recombination occurring due to significant Frank-Condon overlap on higher exciton states, shows that these mechanisms decrease the efficiency of membranes equally on LLI and HLI membranes, therefore, keeping the best performance to HLI.

Nevertheless a more comprehensive study to be presented in the next section taking into account the coupled exciton-RC cycling is able to justify nature’s choice of proceeding with the observed bacterial adaptations.

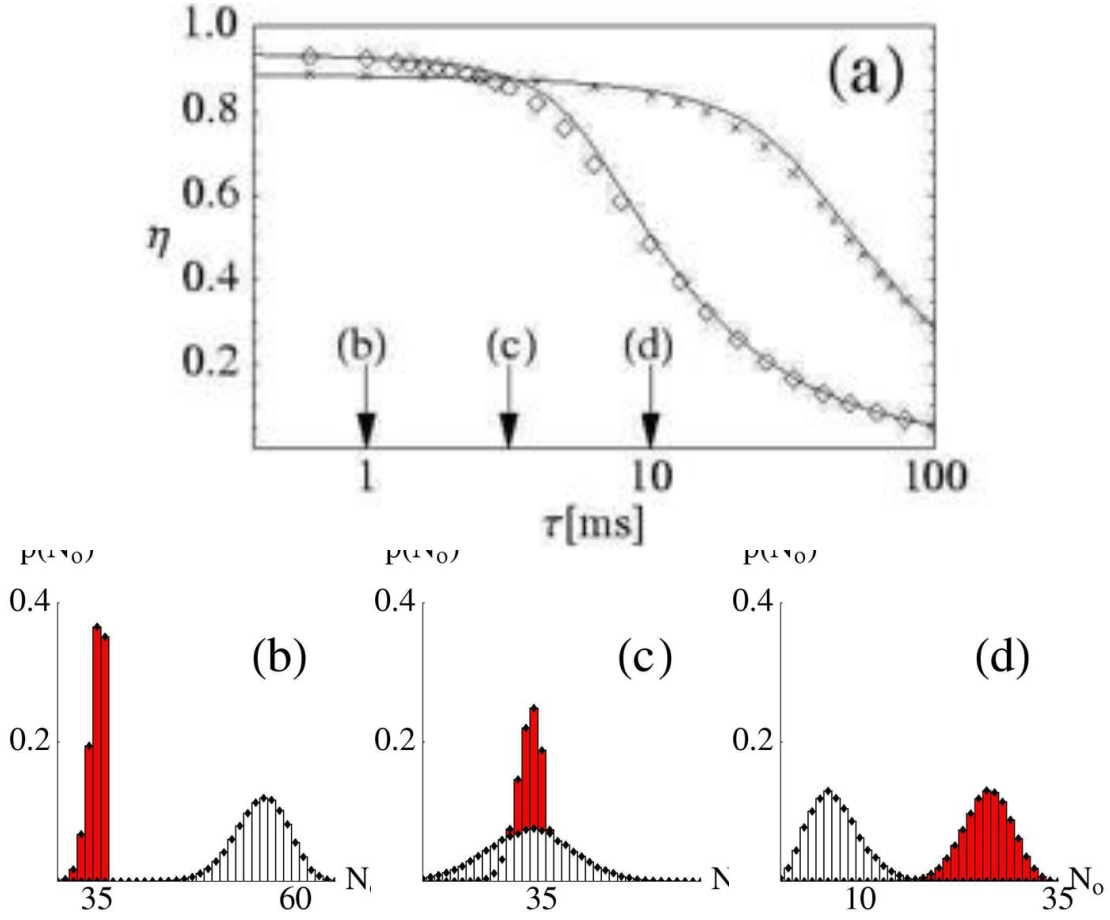


FIG. 13: (a) Monte Carlo calculation of efficiency η of HLI (diamonds) and LLI (crosses) grown membranes, as a function of the RC-cycling time τ . Continuous lines give the result of the analytical model. (b), (c) and (d) show the distributions $p(N_o)$ of the number of open RCs for the times shown with arrows in the main plot for HLI (filled bars) and LLI (white bars).

3. Complete chromatophores: Exciton and RC cycling coupled dynamics.

It has been here repeatedly commented that RCs perform a cycle that provides the required exciton-chemical energy conversion. We now explain that the answer as to how adaptation can prefer the empirically observed HLI and LLI structures under different illumination conditions, lies in the *interplay* between the excitation kinetics and RC cycling dynamics. By virtue of quinones-quinol and cytochrome charge carriers, the RC dynamics features a ‘dead’ (or equivalently ‘busy’) time interval during which quinol is produced, removed and then a new quinone becomes available [26, 28]. Once quinol is produced, it leaves the RC and a new quinone becomes attached. These dynamics are introduced into the simulation algorithm as presented in section , by closing an RC for a (random) poissonian distributed time with mean τ after two excitations form quinol. The cycle can be sketched as follows: open RC \rightarrow 2 ionizing excitations form quinol \rightarrow closed RC in a time with mean τ \rightarrow open RC. This RC cycling time τ implies that at any given time, not all RCs are available for turning the electronic excitation into a useful charge separation. Therefore, the number of useful RCs decreases with increasing τ . Too many excitations will rapidly close RCs, implying that any subsequently available nearby excitation will tend to wander along the membrane and eventually be dissipated - hence reducing η . For the configurations resembling the empirical architectures (Fig.12), this effect is shown as a function of τ in Fig. 13(a) yielding a wide range of RC-cycling times at which LLI membrane is more efficient than HLI. Interestingly, this range corresponds to the measured time-scale for τ of milliseconds [26], and supports the suggestion that bacteria improve their performance in LLI conditions by enhancing quinone-quinol charge carrier dynamics as opposed to manipulating exciton transfer. As mentioned, a recent proposal [35] has shown numerically that the formation of LH2 para-crystalline domains produces a clustering trend of LH1 complexes with enhanced quinone availability – a fact that would reduce the RC cycling time.

However, the crossover of efficiency at $\tau \approx 3$ ms implies that even if no enhanced RC-cycling occurs, the HLI will

be less efficient than the LLI membranes on the observed τ time-scale. The explanation is quantitatively related to the number N_o of open RCs. Figs. 13(b), (c) and (d) present the distribution $p(N_o)$ of open RCs, for both HLI and LLI membranes and for the times shown with arrows in Fig.13(a). When the RC-cycling is of no importance (Fig. 13(b)) almost all RCs remain open, thereby making the HLI membrane more efficient than LLI since having more (open) RCs induces a higher probability for special pair oxidation. Near the crossover in Fig. 13, both membranes have distributions $p(N_o)$ centered around the same value (Fig. 13(c)), indicating that although more RCs are present in HLI vesicles, they are more frequently closed due to the ten fold light intensity difference, as compared to LLI conditions. Higher values of τ (Fig. 13(d)) present distributions where the LLI has more open RCs, in order to yield a better performance when photons are scarcer. Note that distributions become wider when RC cycling is increased, reflecting the mean-variance correspondence of Poissonian statistics used for simulation of τ . Therefore the trade-off between RC-cycling, the actual number of RCs and the light intensity, determines the number of open RCs and hence the performance of a given photosynthetic vesicle architecture (i.e. HLI versus LLI).

Hence, even though these adaptations show such distinct features in the experimentally relevant regimes for the RC-cycling time and illumination intensity magnitude [26, 28, 36], Figs.13(c) and (d) show that the distributions of open RCs actually overlap implying that despite such differences in growing environments, due to the adaptations arising, the resulting dynamics of the membranes become quite similar. Growth conditions generate adaptations that allow on LLI membrane to have a larger number of open RCs than the HLI adaptation and therefore LLI membrane will perform better than HLI with respect to RC ionization irrespective of any funneling dynamics. The inclusion of RC dynamics implies that the absorbed excitation will not find all RCs available, and somehow funneling would limit the chance of a necessary membrane sampling to explore further open RCs. Globally, a given amount of closed RCs will eventually alter the excitation's fate since probable states of oxidization are readily reduced. In a given lifetime, an excitation will find (depending on τ and current light intensity I) a number of available RCs – the *effective stoichiometry* – which is different from the actual number reported by Atomic Force Microscopy [2, 36].

The effect of incident light intensity variations relative to the light intensity during growth with both membranes, presents a similar behavior. In Ref. [5, 6] such study is performed and it is concluded that: the LLI membrane performance starts to diminish well beyond the growth light intensity, while the HLI adaptation starts diminishing just above its growth intensity due to rapid RC closing that induce increased dissipation. Hence, in LLI membranes excess photons are readily used for bacterial metabolism, and HLI membranes exploit dissipation in order to limit the number of processed excitations. In the same work, it is found that the effect of the arrangement itself is lost due to RC dynamics, since the effective stoichiometry with spread out open RCs becomes alike among different membranes sharing the same amount of RCs, equal cycling time τ and incident light intensity.

To summarize so far, the arrangement of complexes slightly changes the efficiency of the membranes when no RC dynamics is included – but with RC dynamics, the most important feature is the number of open RCs. Although the longer RC closing times make membranes more prone to dissipation and decreased efficiency, it also makes the architecture less relevant for the overall dynamics. The relevant network architecture instead becomes the dynamical one including sparse open RCs, not the static geometrical one involving the actual clustered RCs.

4. Analytical model

Within a typical fluorescence lifetime of 1 ns, a single excitation has travelled hundreds of sites and explored the available RCs globally. The actual arrangement or architecture of the complexes seems not to influence the excitation's fate, since the light intensity and RC cycling determine the number of open RCs and the availability for P oxidation.

4.1 Excitation transfer-RC cycling rate model

Here, we present an alternative rate model which is inspired by the findings of the numerical simulations, but which (1) globally describes the excitation dynamics and RC cycling, (2) leads to analytical expressions for the efficiency of the membrane and the rate of quinol production, and (3) sheds light on the trade-off between RC-cycling and exciton dynamics [5, 6].

Shortly, N_E excitations are absorbed by the membrane at a rate γ_A , and will find its way to become RC ionizations with a rate per particle $\lambda_C(N_o)$ whose dependence on the number of open RCs is made explicit, or be dissipated at a rate γ_D . On the other hand, RCs have their own dynamics, closing at a rate $\lambda_C(N_o) \times N_E$ and individually opening at a rate $1/\tau$. The dependence $\lambda_C(N_o)$ is numerically found aided by the stochastic model and shown in Fig.14(a).

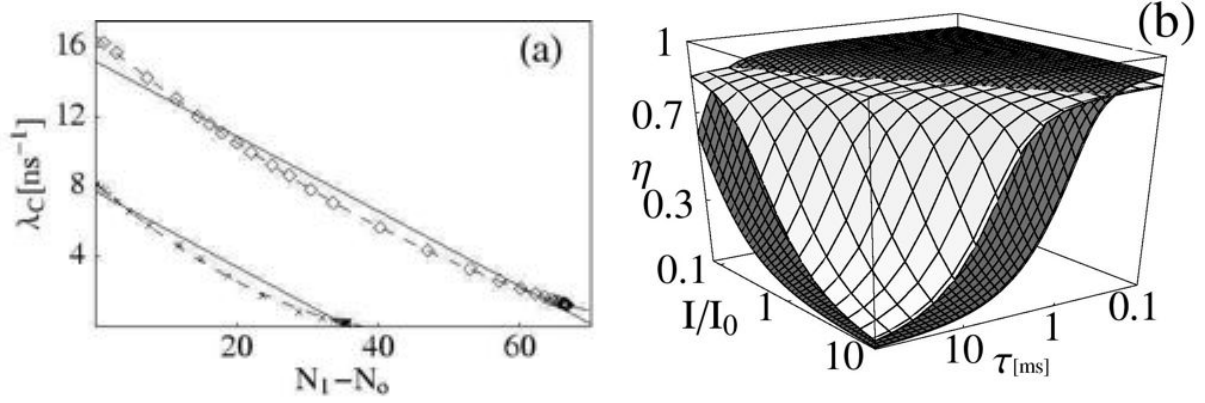


FIG. 14: (a) Numerical results showing the rate of ionization $\lambda_C(N_o)$ of an RC for HLI (diamonds) and LLI (crosses) membranes, together with a quadratic (dashed line) and linear (continuous) dependence on the number of closed RCs ($N_1 - N_o$). The fitting parameters for $a + bN_o$ are $a = \{15.16, 7.72\} \text{ns}^{-1}$, $b = \{-0.21, -0.21\} \text{ns}^{-1}$; and for $a + bN_o + cN_o^2$, $a = \{16.61, 8.21\} \text{ns}^{-1}$, $b = \{-0.35, -0.33\}$, and $c = \{3.6, 1.5\} \mu\text{s}^{-1}$, for HLI and LLI membranes respectively. (b) η as function of τ and $\alpha = I/I_0$, obtained from the complete analytical solution for LLI (white) and HLI (grey) membranes

Rate equations can therefore be written:

$$\frac{dN_E}{dt} = -(\lambda_C(N_o) + \gamma_D)N_E + \gamma_A \quad (23)$$

$$\frac{dN_o}{dt} = \frac{1}{\tau}(N_1 - N_o) - \frac{\lambda_C(N_o)}{2}N_E. \quad (24)$$

to be solved, and of use for the calculation of the steady-state efficiency $\eta = n_{RC}/n_A$:

$$\eta = \frac{\lambda_C(N_o)N_E}{\gamma_A}. \quad (25)$$

A linear fit for $\lambda_C(N_o)$ allows an analytical expression for η :

$$\eta(\tau, \gamma_A(I)) = \frac{1}{\gamma_A \lambda_C^0 \tau} \left\{ 2N_1(\lambda_C^0 + \gamma_D) + \gamma_A \lambda_C^0 \tau - \right. \quad (26)$$

$$\left. \sqrt{4N_1^2(\lambda_C^0 + \gamma_D)^2 + 4N_1\gamma_A\lambda_C^0(\gamma_D - \lambda_C^0)\tau + (\gamma_A\lambda_C^0\tau)^2} \right\} \quad (27)$$

where λ_C^0 is the rate of RC ionization when no RC-cycling is accounted, dependent only on the amount of RCs present in the vesicle [5]. This analytical expression is shown in Fig.14(b) and illustrates that $\eta \geq 0.9$ if the transfer-P reduction time is less than a tenth of the dissipation time, not including RC cycling. As can be seen in Figs. 13(a), the analytical solution is in good quantitative agreement with the numerical stochastic simulation, and provides support for the assumptions made. Moreover, this model shows directly that the efficiency is driven by the interplay between the RC cycling time and light intensity. Figure 14(b) shows up an entire region of parameter space where LLI membranes are better than HLI in terms of causing P ionization, even though the actual number of RCs that they have is smaller. In view of these results, it is interesting to note how clever Nature has been in tinkering with the efficiency of LLI vesicles and the dissipative behavior of HLI adaptation, in order to meet the needs of bacteria subject to the illumination conditions of the growing environment.

4.2 Bacterial metabolic demands

Photosynthetic membranes must provide enough energy to fulfill the metabolic requirements of the living bacteria quantified by the quinol output or quinol rate

$$W = \frac{1}{2} \frac{dn_{RC}}{dt} \quad (28)$$

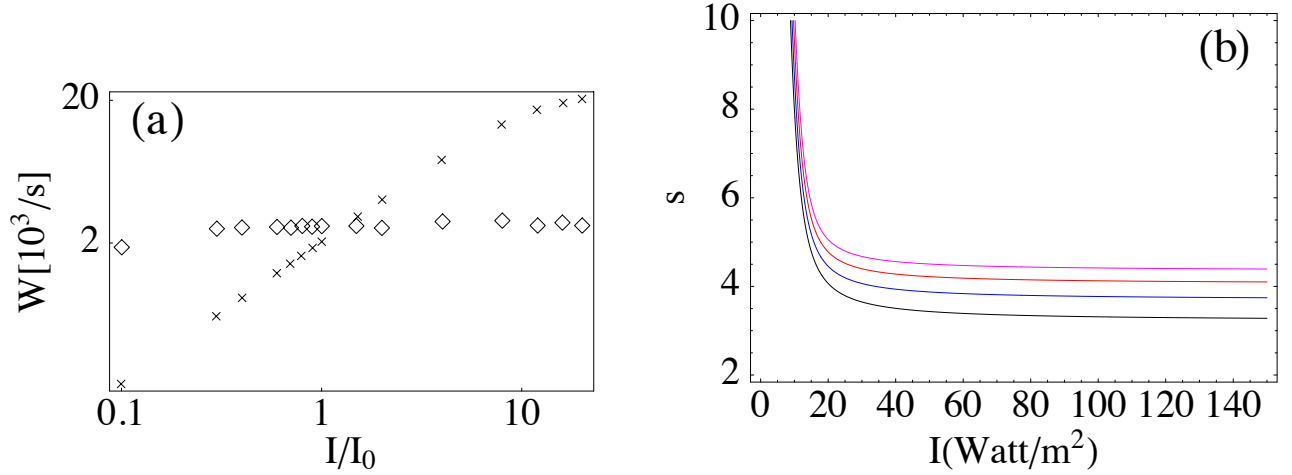


FIG. 15: (a) Quinol rate W in HLI (diamonds, $I_0 = 100 \text{ W/m}^2$) and LLI (crosses, $I_0 = 10 \text{ W/m}^2$) grown membranes, as a function of incident intensity I . (b) Quinol rate contours of $W = \{1900, 2000, 2100, 2200\} \text{ s}^{-1}$ in black, blue, red and pink, respectively.

which depends directly on the excitations that ionize RCs n_{RC} . The factor $\frac{1}{2}$ accounts for the requirement of two ionizations to form a single quinol molecule. Although these membranes were grown under continuous illumination, the adaptations themselves are a product of millions of years of evolution. Using RC cycling times that preserve quinol rate in both adaptations, different behaviors emerge when the illumination intensity is varied (see Fig. 15(a)). The increased illumination is readily used by the LLI adaptation, in order to profit from excess excitations in an otherwise low productivity regime. On the other hand, the HLI membrane maintains the quinone rate constant, thereby avoiding the risk of pH imbalance in the event that the light intensity suddenly increased. We stress that the number of RCs synthesized does not directly reflect the number of available states of ionization in the membrane. LLI synthesizes a small amount of RCs in order to enhance quinone diffusion, such that excess light intensity is utilized by the majority of special pairs. In HLI, the synthesis of more LH1-RC complexes slows down RC-cycling, which ensures that many of these RCs are unavailable and hence be advantageous of evenly distributed dissipation to steadily supply quinol independent of any excitation increase. The very good agreement between our analytic results and the stochastic simulations, yields additional physical insight concerning the stoichiometries found experimentally in *Rsp. Photometricum*.

A closed form expression regarding all dynamical parameters involved can be obtained [5]:

$$2W(s, I) = \frac{\gamma_A(s, I)}{2} + \frac{1}{B(s)} \left(1 + \frac{\gamma_D}{\lambda_e^0}\right) + \sqrt{\left[\frac{\gamma_A(s, I)}{2} + \frac{1}{B(s)} \left(1 + \frac{\gamma_D}{\lambda_e^0}\right)\right]^2 + \frac{\gamma_A(s, I)}{2B(s)}} \quad (29)$$

where the dependence on stoichiometry is made explicit due to absorption cross section in γ_A and on $B(s) = \frac{\tau(s)(A_1 + sA_2)}{f(s)A_0}$, which is a parameter that depends on area $A_{1(2)}$ of individual LH1 (LH2) complexes and filling fraction $f(s)$. The filling chromatophore fraction dependence on s is available from experimental data of Ref.[35] and $\tau(s)$ is constructed from an interpolation scheme [5].

As emphasized in Ref. [34], membranes with $s=6$ or $s=2$ were not observed, which is to be compared with the contour plots regarding constant quinol output, of s as a function of growing light intensity I_0 , shown in Fig.15(b). These results support a dichotomic observation where $s \approx 4$ predominantly on a great range for growing light intensity. However, a prediction can be made for 30-40 W/m^2 where a great sensitivity of stoichiometry ratios rapidly build up the number of antenna LH2 complexes. Very recently [25], membranes were grown with 30 W/m^2 and an experimental stoichiometry of 4.8 was found. The contour of 2200 s^{-1} predicts a value for stoichiometry of 4.72 at such growing light intensities. This agreement is quite remarkable, since a simple linear interpolation among the values $s \approx 4$, $I_0 = 100 \text{ W/m}^2$ and $s \approx 8$, $I_0 = 10 \text{ W/m}^2$ would wrongly predict $s = 7.1$ at 30 W/m^2 . We encourage experimentalists to confirm the full range of predicted behaviors as a function of light-intensity and stoichiometry. Such exercise would without doubt confirm/expand the understanding on RC-exciton dynamics trade off, pinpointing a direction to pursue solar energy conversion research, provided by Nature itself.

4.3 Performance of photosynthetic membranes under extreme photon statistics

Photosynthetic (e.g purple) bacteria provide the crucial coupling between the Sun’s energy and the production of food on Earth, and have adapted successfully to a variety of terrestrial conditions since the beginnings of life on Earth several billion years ago. In this section we explore whether terrestrial bacteria, which are the product of millions of years of evolutionary pressure on Earth, could survive if suddenly exposed to incident light with extreme statistics. We are therefore mimicking a scenario in which purple bacteria are either (i) suddenly transported to some unknown extreme solar environment elsewhere in the universe, or (ii) where our own Sun suddenly picks up extremal behavior in terms of the temporal statistics of its emitted photons, or (iii) the bacteria are subjected to extreme artificial light sources such as that in Ref. [4] involving stimulated Raman scattering, as well as in coherent anti-Stokes Raman scattering in silicon, or (iv) the external membrane skin of the bacterium is modified in such a way that the absorption of photons takes on extreme statistical properties.

Our discussion is qualitatively different from previous work looking at life in extreme conditions, since those discussions have tended to focus on *environmental* extremes affecting the biochemical metabolism or extremes in the incident light intensity. By contrast, our current discussion focuses on extremes in the incident photon statistics. Although the setting is largely hypothetical, our theoretical predictions are based on a realistic semi-empirical model which incorporates (i) high precision empirical AFM information about spatial locations of LH1 and LH2 biomolecular complexes in the membrane architecture of *Rsp. Photometricum* purple bacteria, and (ii) full-scale stochastic simulations of the excitation kinetics and reaction center dynamics within the empirical membrane.

As with any process involving events occurring in a stochastic way over time, the statistical properties of arriving photons may show deviations from a pure coin-toss process in two broad ways: burstiness and memory [15]. First consider the simplest process in which the rate of arrival of a photon has a constant probability per unit time. It is well known that this so-called Poisson process produces a distribution of the waiting time for the next photon arrival which is exponential in form, given by $P_P(\tau) \sim \exp(-\tau/\tau_0)$. The extent to which the observed arrival time distribution $P(\tau)$ deviates from exponential, indicates how non-Poissonian the photon arrival is. Following Barabasi [15], we refer to this as ‘burstiness’ B and define it by its deviation from a purely Poisson process:

$$B \equiv \frac{(\sigma_\tau/m_\tau - 1)}{(\sigma_\tau/m_\tau + 1)} = \frac{(\sigma_\tau - m_\tau)}{(\sigma_\tau + m_\tau)}$$

where σ_τ and m_τ are the standard deviation and mean respectively of the empirical distribution $P(\tau)$. For a pure Poisson process, the mean and standard deviation of the arrival time distribution are equal and hence $B = 0$. The other property which can be noticeable for a non-Poisson process is the memory M between consecutive inter-arrival times which, following Barabasi, we define as:

$$M \equiv \frac{1}{n_\tau - 1} \sum_{i=1}^{n_\tau-1} \frac{(\tau_i - m_1)(\tau_{i+1} - m_2)}{\sigma_1 \sigma_2}$$

where n_τ is the number of inter-arrival times measured from the signal and $m_1(m_2)$ and $\sigma_1(\sigma_2)$ are sample mean and sample standard deviation of $\tau_i(\tau_{i+1})$ ’s respectively ($i = 1, \dots, n_\tau - 1$). For a pure Poisson process, $M = 0$. Both B and M range from -1 to $+1$, with the value $B = 0$ and $M = 0$ for a strict Poisson process. We will assume for simplicity that the arriving photons are all absorbed and hence one exciton created within the membrane by each photon. This can easily be generalized but at the expense of adding another layer of statistical analysis to connect the statistics of arriving photons to the statistics of the excitons being created within the LH2/LH1 membrane – indeed, taking a constant absorption probability less than unity would not change our main conclusions. We will also neglect the possibility that several photons arrive at exactly the same time. In principle, incident photons can be generated numerically with values of B and M which are arbitrarily close to any specific (M, B) value – however this is extremely time-consuming numerically. Instead, we focus here on specific processes where the B and M can be calculated analytically. Although this means that the entire (M, B) parameter space is not accessed, most of it can indeed be – and with the added advantage that analytic values for B and M are generated.

Figure 16 summarizes our findings in terms of the incident photons (i.e. excitation input) and metabolic output from the LH2/LH1 membrane, over the entire (M, B) parameter space. The subspace shown by the combination of the white and dotted regions (i.e. the region in the (M, B) space which is *not* diagonally shaded) comprises points with (M, B) values that can be generated by one of three relatively simple types of photon input: (a) step input, (b) bunched input and (c) power-law step input, as shown in the three panels respectively. Each point in the blank or

dotted region denotes a time-series of initial excitations in the membrane with those particular burstiness and memory values (B and M). This train of initial excitations then migrates within the membrane of LH2/LH1 complexes, subject to the dynamical interplay of migration and trapping as discussed earlier in this paper, and gives rise to a given output time-series of 'food' (quinol) to the bacteria. Figure 16 shows explicitly a variety of initial (M, B) values (crosses and stars) and the trajectory represents the locus of resulting quinol outputs from the reaction centers (RC) for this particular (M, B) input. The trajectory is generated by varying the RC closing time within the range of physically reasonable values. The trajectory is finite since the range of physically reasonable RC closing times is also finite (20 to 1000Hz). As the time during which the RC is closed increases, the output becomes more Poisson-like, i.e. the B and M output values from the membrane after absorption at the RC, tend towards 0. Hence the trajectories head toward the center as shown.

The (M, B) values for natural sunlight on Earth lie near $M = 0$ and $B = 0$ since the incident photon arrival from the Sun is approximately a Poisson process. This produces a quinol output which is also a Poisson process ($M = 0$ and $B = 0$). Now suppose a terrestrial bacteria is suddenly subjected to an extreme incident light source with (M, B) values which lie at a general point in (M, B) parameter space. Can it survive? It is reasonable to expect that the bacteria will not survive if the resulting quinol output is very different from that on Earth (i.e. very different from $B = 0$ and $M = 0$) since the bacteria is well-tuned for Life on Earth only. Hence we say that the bacteria can only survive if the quinol output has (M, B) values within 0.01 of the terrestrial values of $B = 0$ and $M = 0$. The blank spaces denote (M, B) values for which the bacteria would survive, while the dotted spaces are where the bacteria would die.

Remarkably, there are therefore substantial regions of extreme incident photon statistics (i.e. $B \neq 0$ and $M \neq 0$) where the bacteria would survive, producing a quinol output for the rest of the organism which resembles that on Earth (i.e. $|B| < \epsilon$ and $|M| < \epsilon$ where $\epsilon = 0.01$). The fact that these blank spaces have an irregular form is due to the highly nonlinear nature of the kinetic interplay between exciton migration and trapping, as discussed earlier in this chapter. For example, panel (c) shows that a bacterium which is only tuned to survive on Earth can have a maximally negative burstiness $B = -1$ and a maximal memory $M = 1$, meaning that the incident photons arrive like the regular ticks of a clock. The same applies to all the incident photon conditions demonstrated by the blank spaces. If we make the survival criterion more generous (i.e. $\epsilon > 0.01$) the blank spaces corresponding to survivability of the terrestrial bacterium increase in size until no dotted space remains (i.e. when $\epsilon = 1$). All the dotted areas in Fig. 16 become blank spaces and hence represent survivable incident photon conditions for the bacteria.

5. Perspectives: Photosynthetic membranes of purple bacteria as a basis to develop stable energy conversion

This chapter has covered a comprehensive review of purple bacteria adaptation to light intensity conditions and has provided a basis to understand the chromatic adaptation of photosynthetic harvesting membranes as a consequence of the requirement imposed by nature on living organisms to develop a machinery capable of fuel production in a stable manner. It is worth to emulate, and certainly interesting to develop in artificial devices to surpass the usual bleaching on semiconductor panels, an analogous mechanism to the excitation kinetics and RC dynamics interplay, in order to shift the emphasis of requirements of fuel production and allow highly efficient energy transfer to available charge carriers (quinones) in low light intensity conditions, while consistently, a leveled fuel (quinol) production statistics is accomplished when photon arrival varies both in intensity and photon waiting time statistics.

Acknowledgments

The authors acknowledges financial support from Research Projects Facultad de Ciencias, Universidad de los Andes, Banco de la Republica and Fundacion Mazda.

-
- [1] Arellano, J. B., Raju, B. B., Nakvi, K. R. and Gilbro, T. [1998]. Estimation of pigment stoichiometries in photosynthetic systems of purple bacteria: special reference to the (absence of) second carotenoid in LH2, *Photochemistry and Photobiology* 68: 84.
 - [2] Bahatyrova, S., Freese, R. N., Siebert, C. A., Olsen, J. D., van der Werf, K. A., van Grondelle, R., Niederman, R. A., Bullough, O. A., Otto, C. and Hunter, N. C. [2004]. The native architecture of a photosynthetic membrane, *Nature* 430: 1058.

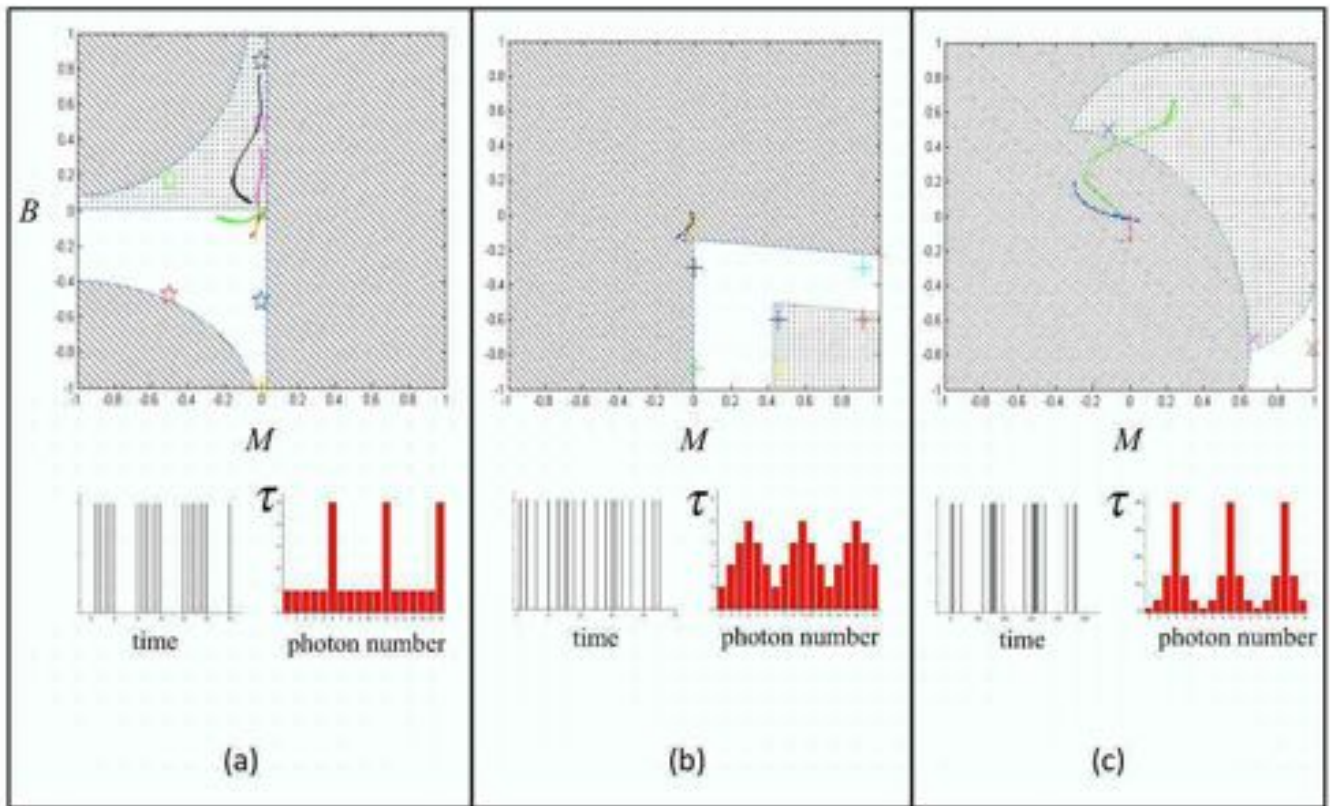


FIG. 16: The (M, B) phase diagram governing survivability of a terrestrial bacteria under a wide range of incident photon time-series with a given burstiness B and memory M . The sum of the blank and dotted areas in each diagram is the region accessible by each of the three photon processes shown. For each (M, B) value, a time-series of photons is created with these properties and used to generate excitations within the membrane. The resulting quinol output time-series is then calculated. Assuming that this output needs to be similar to that on Earth, the dotted region corresponds to photon (M, B) input values for which the bacteria would die, while the blank region corresponds to photon input for which the bacteria would survive. The trajectories represent the range of quinol outputs from the reaction centers (RC) as we span the range of physically reasonable RC closure times, given a particular input (shown as a star or cross of the same color). As the time during which the RC is closed increases, the B and M output values tend to move toward the origin (i.e. toward $B = 0$ and $M = 0$). Bottom: Photon inputs correspond to (a) step input, (b) bunched input and (c) power-law step input. Lower row in each case shows photon arrival process (left, black barcode) and waiting time τ between photon arrivals (right, red histogram).

- [3] Borisov, A. Y., Freiberg, M., Godik, V. I., K., R. K. and Timpmann, K. E. [1985]. Kinetics of picosecond bacteriochlorophyll luminescence in vivo as a function of the reaction center state, *Biochimica et Biophysica Acta* 807: 221.
- [4] Borlaug, D., Fathpour, S. and Jalali, B. [2009]. Extreme value statistics in silicon photonics, *IEEE Photonics Journal* 1: 1.
- [5] Caycedo-Soler, F., Rodríguez, F., Quiroga, L. and Jonhson, N. [2010a]. Interplay between excitation kinetics and reaction-center dynamics in purple bacteria, *New Journal of Physics* 12: 095008.
- [6] Caycedo-Soler, F., Rodríguez, F., Quiroga, L. and Jonhson, N. [2010b]. Light-Harvesting Mechanism of Bacteria exploits a critical interplay between the dynamics of transfer and trapping, *Phys. Rev. Lett.* 104: 158302.
- [7] Codgell, R. J., Gall, A. and Kohler, J. [2006]. The architecture and function of the light-harvesting apparatus of purple bacteria: From single molecule to in vivo membranes, *Quart. Rev. Biophys.* 39: 227–324.
- [8] Comayras, F., Jungas, C. and Lavergne, J. [2005]. Functional consequences of the organization of the photosynthetic apparatus in rhodobacter sphaeroides. i. quinone domains and excitation transfer in chromatophores and reaction center antenna complexes, *J. Biol. Chem.* 280: 11203–11213.
- [9] Engel, G., Calhoun, T., Read, E., Ahn, T., Mancal, T., Cheng, Y., Blankenship, R. and Fleming, G. [2007]. Evidence for wavelike energy transfer through quantum coherence in photosynthetic systems, *Nature* 446: 782–786.
- [10] Fleming, G. R., Martin, J. L. and Breton, J. [1988]. Rates of primary electron transfer in photosynthetic reaction centres and their mechanistic implications, *Nature (London)* 333: 190.
- [11] Förster, T. [1965]. *Delocalized excitation and excitation transfer*, Academic Press, New York.
- [12] Francke, C. and Amesz, J. [1995]. The size of the photosynthetic unit in purple bacteria., *Photosynthetic Res.* 46: 347.
- [13] Gall, A., Gardiner, A. R., Gardiner, R. J. and Robert, B. [2006]. Carotenoid stoichiometry in the LH2 crystal: no spectral

- evidence for the presence of the second molecule on the $\alpha\beta$ -apoprotein dimer, *FEBS Letters* 580: 3841.
- [14] Geyer, T. and Heims, V. [2006]. Reconstruction of a Kinetic model of the Chromophores Vesicles from Rhodospirillum rubrum, *Biophysical Journal* 91: 927.
- [15] Goh, K. and Barabasi, A. [2008]. Burstiness and memory in complex systems, *Europhys. Lett.* 81.
- [16] Hess, S., Cachisvilis, M., Timpmann, K. E., Jones, M., Fowler, G., Hunter, N. C. and Sundstrom, V. [1995]. Temporally and spectrally resolved subpicosecond energy transfer within the peripheral antenna complex (lh2) and from lh2 to the core antenna complex in photosynthetic purple bacteria, *Proceedings National Academy of Sciences* 92: 12333.
- [17] Hu, X., Ritz, T., Damjanovic, A., Autenrie, F. and Schulten, K. [2002]. Photosynthetic apparatus of purple bacteria., *Quart. Rev. of Biophys.* 35: 1–62.
- [18] Hu, X., Ritz, T., Damjanović, A. and Schulten, K. [1997]. Pigment Organization and Transfer of Electronic Excitation in the Photosynthetic Unit of Purple Bacteria, *Journal of Physical Chemistry B* 101: 3854–3871.
- [19] Jamieson, S. J. and al, e. [2002]. Projection structure of the photosynthetic reaction centre-antenna complex of *Rhodospirillum rubrum* at 8.5 Å resolution., *EMBO Journal* 21: 3927.
- [20] Jang, S., Newton, M. D. and Silbey, R. J. [2004]. Multichromophoric Förster Resonance Energy Transfer, *Phys. Rev. Lett.* 92: 218301.
- [21] Jang, S., Newton, M. D. and Silbey, R. J. [2007]. Multichromophoric Förster resonance energy transfer from b800 to b850 in the light harvesting complex 2: Evidence for subtle energetic optimization by purple bacteria, *J. Phys. Chem. B* 111: 6807–6814.
- [22] Karrasch, S., Bullough, P. A. and Ghosh, B. [1995]. The 8.5 Å projection map of the light harvesting complex I from *Rhodospirillum rubrum* reveals a ring composed of 16 subunits, *EMBO Journal* 14: 631.
- [23] Lee, H., Cheng, Y. and Fleming, G. [2007]. Coherence dynamics in photosynthesis: Protein protection of excitonic coherence, *Science* 316: 1462.
- [24] Lia, Y., DiMagno, T. J. Chang, T. C., Wang, Z., Du, M., Hanson, D. K., Schiffer, M., Norris, J. R., R., F. G. and Popov, M. S. [1993]. Inhomogeneous electron transfer kinetics in reaction centers of bacterial photosynthesis, *J. Phys. Chem.* 97: 13180.
- [25] Liu, L., Duquesne, K., Sturgis, J. and Scheuring, S. [2009]. Quinone pathways in entire photosynthetic chromatophores of rhodospirillum rubrum, *J. Mol. Biol* 27: 393.
- [26] Milano, F., A., A., Mavelli, F. and Trotta, M. [2003]. Kinetics of the quinone binding reaction at the qb site of reaction centers from the purple bacteria rhodospirillum rubrum reconstituted in liposomes, *Eur. Journ. Biochem* 270: 4595.
- [27] McDermott, G., Prince, S. M., Freer, A. A., Hawthornthwaite-Lawless, A. M., Papiz, M. Z. and Cogdell, J. [1995]. Crystal structure of an integral membrane light-harvesting complex from photosynthetic bacteria, *Nature* 374: 517.
- [28] Osváth, S. and Maróti, P. [1997]. Coupling of cytochrome and quinone turnovers in the photocycle of reaction centers from the photosynthetic bacterium rhodospirillum rubrum, *Biophys. Journ* 73: 972–982.
- [29] Panitchayangkoona, G., Hayes D., Fransteda, K. A., Caram J. R., Harel, E., Wen, J., Blankenship, R. and Engel, G. S. [2010]. Long-lived quantum coherence in photosynthetic complexes at physiological temperature, *PNAS* 107: 12766–12770.
- [30] Pfenning, N. [1978]. *The Photosynthetic Bacteria*, Plenum Publishing Corporation, New York.
- [31] Ritz, T., Park, S. and Schulten, K. [2001]. Kinetics of exciton migration and trapping in the photosynthetic unit of purple bacteria, *Journal of Physical Chemistry B* 105: 8259.
- [32] Roszack, A. W. and et al [2003]. Crystal Structure the RC-LH1 core complex from Rhodospseudomonas palustris, *Science* 302: 1969.
- [33] Scheuring, S., Rigaud, J. L. and Sturgis, J. N. [2004]. Variable lh2 stoichiometry and core clustering in native membranes of rhodospirillum rubrum, *EMBO* 23: 4127.
- [34] Scheuring, S. and Sturgis, J. [2005]. Chromatic adaptation of purple bacteria, *Science* 309: 484.
- [35] Scheuring, S. and Sturgis, J. N. [2006]. Dynamics and diffusion in photosynthetic membranes from rhodospirillum rubrum, *Biophys. J.* 91: 3707.
- [36] Scheuring, S., Sturgis, J. N., Prima, V., Bernadac, Levi, D. and Rigaud, J. L. [2004]. Watching the photosynthetic apparatus in native membranes, *Proceeding of National Academy of Sciences USA* 101: 1193.
- [37] Scully, M. O. and Zubairy, M. S. [1997]. *Quantum Optics*, Cambridge University Press.
- [38] Shreve, A. P., Trautman, J. K., Franck, H. A., Owens, T. G. and Albrecht, A. C. [1991]. Femtosecond energy-transfer processes in the b800-b850 light-harvesting complex of rhodospirillum rubrum 2.4.1, *Biochimica et Biophysica Acta* 1058: 280–288.
- [39] Timpmann, K., Freiberg, A. and Sundström, V. [1995]. Energy trapping and detrapping in the photosynthetic bacterium rhodospseudomonas viridis: transfer to trap limited dynamics, *Chemical Physics* 194: 275.
- [40] Timpmann, K., Zhang, F., Freiberg, A. and Sundström, V. [1993]. Detrapping of excitation energy transfer from the reaction center in the photosynthetic purple bacterium rhodospirillum rubrum, *Biochemical et Biophysica Acta* 1183: 185.
- [41] van Amerongen, H., Valkunas, L. and R. G. [2000]. *Photosynthetic Excitons*, World Scientific Publishing Co., Singapore.
- [42] van Grondelle, R., Dekker, J., Gillbro, T. and Sundstrom, V. [1994]. Energy transfer and trapping in photosynthesis, *Biochim. et Biophys. Acta* 11087: 1–65.
- [43] Visscher, K., Bergström, H., Sundstrom, V., Hunter, C. and van Grondelle, R. [1989]. Temperature dependence of energy transfer from the long wavelength antenna bchl-896 to the reaction center in rhodospirillum rubrum, rhodospirillum rubrum (w.t. and m21 mutant) from 77 to 177k, studied by picosecond absorption spectroscopy, *Photosynthesis Research* 22: 211.
- [44] Visscher, K. J., Chang, M. C. van Mourik, F., Parkes-Loach, P. S., Heller, B. A., Loach, P. A. and van Grondelle, R. [1991]. Fluorescence polarization and low-temperature absorption spectroscopy of a subunit form of light harvesting complex I

from purple photosynthetic bacteria, *Biochemistry* 30: 5734.

- [45] Waltz, T., Jamieson, S. J., Bowers, C. M., Bullough, P. A. and Hunter, C. N. [1998]. *Projection structure of three photosynthetic complexes from Rhodospirillum rubrum: LH2 at 6 Å, LH1 and RC-LH1 at 25 Å* 282: 883.